Droplet Concentration and Spectral Broadening in Southeast Pacific Stratocumulus Clouds

JEFFERSON R. SNIDER, DAVID LEON, AND ZHIEN WANG

Department of Atmospheric Science, University of Wyoming, Laramie, Wyoming

(Manuscript received 28 January 2016, in final form 27 October 2016)

ABSTRACT

Several airborne field experiments have been conducted to verify model descriptions of cloud droplet activation. Measurements of cloud condensation nuclei and updraft are inputs to a parcel model that predicts droplet concentration and droplet size distributions (spectra). Experiments conducted within cumulus clouds have yielded the most robust agreement between model and observation. Investigations of stratocumulus clouds are more varied, in part because of the difficulty of gauging the effects of entrainment and drizzle on droplet concentration and spectra. Airborne lidar is used here to supplement the approach used in prior studies of droplet activation in stratocumulus clouds.

A model verification study was conducted using data acquired during the Southern Hemispheric VAMOS Ocean–Cloud–Aerosol–Land Study Regional Experiment. Consistency between observed and modeled droplet concentrations is achieved, but only after accounting for the effects of entrainment and drizzle on concentrations produced by droplet activation. In addition, predicted spectral dispersions are 74% of the measured dispersions following correction for instrument broadening. This result is consistent with the conjecture that differential activation (at cloud base) and internal mixing (i.e., mixing without entrainment) are important drivers of true spectral broadening.

1. Introduction

Planetary albedo, the fraction of solar input reflected by the Earth system, is controlled by many phenomena and has a profound impact on weather and climate (Charlson et al. 2005, and references therein). Marine stratocumulus clouds are one of the most important contributors to planetary albedo. Also, because these clouds occur low in the atmosphere and are relatively warm, the cooling they provide by reflecting at solar wavelengths is not strongly compensated by a radiative effect occurring at infrared wavelengths (Paltridge 1980; Klein and Hartmann 1993). The global impact of marine stratocumulus is recognized because they cover a substantial fraction of the ocean, reflecting sunlight that would otherwise be absorbed. It is also known that the albedo of stratocumulus (Twomey 1977) and their propensity to form rain (Albrecht 1989) can be altered by anthropogenically and naturally produced aerosols. Prediction of that alteration requires understanding of several phenomena: 1) processes that put cloud condensation nuclei (CCN) into the atmosphere, 2) the activation process that converts CCN to cloud droplets, 3) processes that reduce cloud droplet concentrations (entrainment and precipitation), and 4) processes that alter CCN distributions, commonly known as CCN activation spectra.

Both observational and modeling studies have probed how CCN activation spectra influence cloud droplet number concentrations N and thus impact stratocumulus albedo and precipitation. Typically, field observations initialize an activation model, and the output is compared to N measurements. Several parcel model schemes have been developed for describing N as a function of CCN spectrum and updraft (Twomey 1959; Leaitch et al. 1986; Yum et al. 1998; Snider et al. 2003), and some have been implemented as parameterizations within multidimensional cloud models (Ghan et al. 1997; Meskhidze et al. 2005).

All of the aforementioned N-closure studies were complicated by the difficulty of measuring N simultaneous with below-cloud CCN measurements. Brenguier et al. (2000) addressed this by deploying three aircraft in a staggered configuration. In addition, some ground-based investigations of coastal stratocumulus have exploited remote sensing for retrieving N simultaneous with surface

TABLE 1. Definitions used for averaged cloud droplet concentrations and PDF widths. The generic cloud droplet concentration is given by N.

Symbols	Definitions	Averaging interval	Equation or section where defined
$\langle N_{obs} \rangle$ and σ_{obs}	Averaged observed concentration and PDF width	In-cloud segment	Section 4a
$\langle N_{ret} \rangle$ and σ_{ret}	Averaged lidar-retrieved concentration and PDF width	Below-cloud segment	Section 5b
$\langle N_{mod} \rangle$ and σ_{mod}	Unweighted model-averaged concentration and PDF width	Below-cloud segment	Eqs. (5a) and (5c)
$\langle N_{mod,w} \rangle$ and $\sigma_{mod,w}$	Updraft-weighted model-averaged concentration and PDF width	Below-cloud segment	Eqs. (5b) and (5d)

measurements of CCN (e.g., McComiskey et al. 2009). The multiple-aircraft approach has the disadvantage of being expensive, while ground-based coastal investigations may be unrepresentative of conditions offshore (O'Dowd et al. 2014). Airborne remote sensing, with lidar and radar, can help alleviate some of these complications.

Because it also affects albedo and precipitation, the shape of droplet size distributions or spectra have also been the focus of observational and modeling studies in stratocumulus (Hudson and Svensson 1995; Hudson and Yum 1997; Liu and Daum 2002; Liu and Daum 2004; Pawlowska et al. 2006; Lu and Seinfeld 2006; Hudson et al. 2015). Various methods have predicted the standard deviation σ_D of droplet diameter and the average droplet diameter $\langle D \rangle$. In parcel model simulations, both σ_D and the spectral dispersion $\sigma_D/\langle D \rangle$ decrease upward from a few tens of meters above cloud base (Warner 1969; Rogers and Yau; 1989; Hudson and Yum; 1997). Measurements of cloud droplet spectra obtained in stratiform clouds generally do not conform to these predictions [see Miles et al. (2000) for a review], and there is a body of work indicating that a component of this disagreement is broadening by instruments used to make the spectral measurements (Cerni 1983; Politovich 1993; Brenguier and Chaumat 2001). Using models, Cooper (1989) and Cooper et al. (2013) demonstrated how true spectral broadening can result when parcels entering cloud base at differing updrafts, resulting in differing N, come into contact and become mixed. This mechanism was investigated in studies of cumulus (Politovich 1993; Hudson et al. 2012) and in studies of stratocumulus (Hudson and Svensson 1995; Hudson and Yum 1997).

Using airborne measurements of CCN, updraft and cloud microphysical properties, we extend the observations and analyses of the latter two publications. We also compare model predictions of N to values observed within clouds and retrieved using lidar. Our dataset was collected within one of Earth's four climatologically relevant marine stratocumulus cloud sheets, and our use of airborne lidar for N retrieval is unique.

This paper is organized as follows: section 2 describes the airborne instrumentation; section 3 describes the field project, flight patterns, and our selection of 36 analysis intervals; section 4 describes the in-cloud and below-cloud measurements; section 5 describes the airborne remote sensing; and section 6 describes the activation modeling. In section 7, we analyze correlations between predicted and observed values of N and correlations between predicted and observed spectral dispersions. Section 8 summarizes our findings.

Our analysis is based on averages and standard deviations derived for specified intervals of flight data. Droplet concentrations averaged over these intervals are indicated by $\langle N_{obs} \rangle$ (observed), $\langle N_{mod} \rangle$ (modeled), and $\langle N_{ret} \rangle$ (lidar retrieved), and the corresponding standard deviations are symbolized by σ_{obs} (observed), σ_{mod} (modeled), and σ_{ret} (lidar retrieved). These statistics are further defined in Table 1. Henceforth, we refer to the three standard deviations (i.e., σ_{obs}, σ_{mod}, and σ_{ret}) as probability distribution function (PDF) widths.

2. Airborne instruments

Three optical particle counters (OPCs) and one optical array probe (OAP) were used to make measurements of aerosol, droplet, and drizzle spectra: 1) a Passive Cavity Aerosol Spectrometer Probe (PCASP) for dried aerosol particles measured below cloud (diameter D between 0.11 and $3\,\mu m$), 2) a model 300 Forward Scattering Spectrometer Probe (F300) for haze particles measured below cloud ($0.4 < D < 17\,\mu m$), 3) a cloud droplet probe (CDP; $2 < D < 50\,\mu m$) for droplets, and 4) a 2D-C OAP for drizzle drops ($62 < D < 1590\,\mu m$). Laboratory calibrations of the PCASP and the F300 are described in appendix B. Airborne CDP measurements are compared to a model 100 Forward Scattering Spectrometer Probe (F100; $3 < D < 40\,\mu m$) and a particle volume monitor (PVM; Gerber et al. 1994) in section 4a. The first of these comparisons is only available for the last 3 of 14 flights.[1] Starting with 1-s CDP spectral measurements, corresponding to 110 m (assuming the nominal flight speed),

---

[1] A structurally modified F100 was flown in the first 11 flights. Because this instrument's first seven sizing channels are invalidated in the archive data, making its minimum detectable diameter $11\,\mu m$, data from the modified F100 were not used.

we average concentration, liquid water content (LWC), PDF width, and dispersion over specified flight intervals. These averages are a basis for our analysis.

Measurements of the cumulative CCN spectrum, at relatively large values of critical supersaturation ($0.1\% <$ SS $< 2\%$), were derived using the Wyoming static diffusion instrument (Snider et al. 2006, 2010). This instrument sampled air via a forward-facing, isokinetic, solid diffuser inlet (Shank et al. 2012). The average time required for a CCN measurement was 50 s. This is larger than at a fixed SS (30 s) for two reasons: 1) additional time required to vary SS and 2) some CCN measurements were discarded because of drizzle. Criteria used to discard a CCN measurement are provided in section 3.

The upward-pointing Wyoming Cloud lidar (Z. Wang et al. 2009, 2012) was used to retrieve N. The lidar transmits in the near ultraviolet (wavelength $\lambda = 0.355\,\mu m$) at a pulse repetition frequency of 20 Hz. Seven lidar shots were averaged, making the time between samples 0.35 s. The vertical resolution of the lidar is 3.75 m.

Remotely sensed values of cloud-top altitude z_{ct}, retrieved by the Wyoming Cloud Radar (Zuidema et al. 2012), lidar retrievals of cloud-base altitude z_{cb} (Platt et al. 1994), and measurements of cloud-base temperature T_{cb} from an upward-viewing radiometric temperature sensor (RSTT) were also used in our analysis. The RSTT random error is $\pm 0.5\,K$ (Zuidema et al. 2012). This measurement can also be biased by water vapor below cloud base and by the instrument's slow response ($1/e$ response time $\sim 5\,s$). In addition to RSTT, values of both T_{cb} and cloud-base pressure P_{cb} were retrieved from z_{cb} and in situ measurements of temperature, pressure, and altitude. For the latter calculations, it was assumed that the layer between the aircraft and cloud base was well mixed (i.e., $\partial\theta/\partial z = 0$, where θ is potential temperature).

Dewpoint temperatures measured by a chilled-mirror hygrometer were increased by $0.8°C$ to account for a known bias (Bretherton et al. 2010; Zuidema et al. 2012). Measurements of vertical velocity w came from a radome system (Brown et al. 1983). We analyze 1-s measurements of w.

3. Flight patterns and data selection

Data were collected onboard the National Center for Atmospheric Research (NCAR) C-130 aircraft during the VAMOS Ocean–Cloud–Aerosol–Land Study (VOCALS) Regional Experiment (Rex) (Wood et al. 2011a). During October and November 2008, the C-130 conducted 14 long-duration flights. Our focus is on level-flight measurements made below and within the southeastern Pacific stratocumulus deck. By applying criteria explained in this section, 36 analysis intervals, each with three subintervals,

were selected. The subintervals are 1) a level below-cloud flight segment, 2) a level in-cloud flight segment, and 3) an above-cloud segment. Most of the paired below-cloud and in-cloud segments (31 out of 36) were proximate in time ($<30\,min$) but horizontally separated by $\sim 100\,km$. We analyzed 10 of 14 VOCALS flights (Table 2). Flights were excluded because of the unavailability of the PCASP [research flight (RF) 03], the CDP (RF04), the Wyoming CCN instrument (RF11), or the Wyoming Cloud lidar (RF09). When selecting aerosol and CCN measurements from the below-cloud segments, we applied two data-acceptance criteria: 1) $N < 10\,cm^{-3}$ and 2) drizzle drop concentration $< 1\,L^{-1}$.

Figures 1a and 1b show 1 of the 36 analysis intervals in our dataset. This example, from RF05, is used throughout to illustrate our methods. The flight direction on this day was principally east–west with 10-min duration segments below and inside the stratocumulus deck. RF05 is representative of the VOCALS 20°S pattern (Bretherton et al. 2010). Flights utilizing two other patterns were also analyzed. These are the "pollution survey" and the pockets of open cells (POCs) patterns (Wood et al. 2011a). The latter are termed a "POC drift" pattern. Sampling conducted during the pollution survey pattern was similar to that in Figs. 1a and 1b, but with the aircraft directed north–south along $\sim 74°W$ and extending from 20° to 30°S. There are three pollution survey analysis intervals in our dataset. Sampling during the POC-drift pattern was along stacked flight tracks. These were oriented perpendicular to the mean boundary layer wind and were flown below and inside the cloud layer. Subsequent sets of POC-drift tracks were advected downwind by an amount that was several kilometers larger than the mean advection (Wood et al. 2011b). For our analysis of the POC-drift patterns, we define a below-cloud and an in-cloud flight segment so that they nearly overlap in the horizontal. There are five POC-drift analysis intervals in our dataset. For these, the delay between the in-cloud and below-cloud segments varied between 45 and 75 min.

4. In situ measurements

a. LWC, droplet concentration, and spectral dispersion

Here we describe the degree of agreement between CDP and PVM measurements of LWC, between CDP and F100 measurements of concentration, and between CDP and F100 measurements of dispersion. The latter two comparisons are only available for RF12, RF13, and RF14 (section 2). Throughout this paper only those OPC (i.e., CDP or F100) and PVM measurements

TABLE 2. Summary of analyzed dataset. Dashes mean the factor is not available (see section 7c).

Analysis interval	In-cloud start (UTC)	In-cloud end UTC)	Avg observed droplet concentration ($\langle N_{\mathrm{obs}}\rangle$; cm^{-3})	Below-cloud start (UTC)	Below-cloud end (UTC)	Avg vertical velocity ($\langle w\rangle$; m s^{-1})	Std dev of vertical velocity (σ_w; m s^{-1})
RF01–01	1937	1946	183	1914	1927	−0.07	0.47
RF01–02	1806	1811	155	1747	1757	0.09	0.43
RF01–03	1848	1856	159	1829	1843	−0.03	0.40
RF02–01	1338	1342	316	1346	1357	0.24	0.45
RF02–02	1415	1423	271	1428	1438	0.15	0.40
RF02–03	1510	1514	203	1523	1533	0.05	0.47
RF02–04	1551	1600	150	1605	1608	0.05	0.40
RF02–05	1812	1825	110	1710	1720	0.02	0.40
RF02–06	1849	1857	176	1902	1911	−0.00	0.36
RF05–01	0707	0710	231	0721	0731	0.16	0.37
RF05–02	0747	0748	91	0803	0813	0.08	0.39
RF05–03	0846	0855	91	0901	0911	0.16	0.43
RF05–04	0931	0939	95	0945	0954	0.02	0.48
RF05–05	1013	1021	90	1028	1041	0.05	0.55
RF05–06	1113	1117	87	1127	1137	0.05	0.47
RF05–07	1159	1207	100	1212	1223	0.02	0.44
RF05–08	1256	1306	96	1312	1323	0.04	0.45
RF05–09	1343	1353	155	1357	1407	0.06	0.46
RF05–10	1439	1449	229	1454	1500	−0.03	0.35
RF06–02	1036	1045	98	0934	0938	0.07	0.53
RF07–01	1229	1238	93	1243	1248	−0.16	0.47
RF07–02	1313	1318	144	1326	1334	−0.02	0.33
RF08–03	0813	0822	146	0829	0836	0.10	0.47
RF08–04	1117	1124	264	1013	1017	0.10	0.33
RF08–05	1254	1302	171	1308	1318	−0.01	0.29
RF08–06	1358	1408	180	1345	1352	−0.03	0.31
RF10–02	1017	1026	72	1032	1041	0.07	0.35
RF10–03	1100	1109	77	1114	1124	0.02	0.38
RF12–01	1325	1335	266	1339	1348	0.12	0.45
RF12–02	1501	1510	158	1514	1524	0.12	0.29
RF12–03	1551	1600	151	1602	1616	0.04	0.18
RF13–01	1425	1428	149	1432	1442	0.11	0.26
RF13–02	1521	1522	52	1525	1535	0.14	0.29
RF13–03	1815	1817	16	1704	1709	0.06	0.31
RF14–01	1515	1525	196	1529	1534	0.13	0.29
RF14–02	1740	1744	50	1652	1706	0.05	0.22
Std dev			69			0.08	0.09
Max			316			0.24	0.55
Min			16			−0.16	0.18
Mean			146			0.06	0.39
Median			149			0.05	0.40

associated with an LWC > 0.02 g m^{-3} are used in the calculations. We summarize the instrument comparisons by providing a range of the relative difference among the cloud segment averages.

A comparison of LWC values, from the CDP and PVM, is provided in Fig. 2. The relative differences vary between −35% and +35%. The largest relative differences occurred from RF12 to RF14; for these eight comparisons, $\langle\mathrm{LWC}_{\mathrm{CDP}}\rangle$ consistently exceeded $\langle\mathrm{LWC}_{\mathrm{PVM}}\rangle$ (Fig. 2).

Segment-averaged concentrations, derived using the CDP and the F100, agreed within ±10% and the segment-averaged dispersions agreed within ±30%. In these comparisons, there is no evidence of the consistently larger CDP average seen in the RF12–RF14 LWC comparisons.

The measured dispersions were corrected for instrument broadening by applying the technique developed by Politovich (1993). First, we derived a limiting relationship between σ_D and $\langle D\rangle$ for each of our 36 in-cloud segments. Second, this relationship was used to correct the measured values of σ_D as described in Politovich (1993). Third, the corrected dispersions were

TABLE 2. *Extended*

Fitted parameter in $n(SS) = C \times SS^k$ (C; cm^{-3})	Fitted parameter in $n(SS) = C \times SS^k$ (k)	Avg retrieved droplet concentration ($\langle N_{ret} \rangle$; cm^{-3})	Avg modeled droplet concentration [Eq. (5a); $\langle N_{mod} \rangle$; cm^{-3}]	Avg modeled droplet concentration [Eq. (5b); $\langle N_{mod,w} \rangle$; cm^{-3}]	Effective supersaturation (SS_{eff}, %)	Correction factor (CF)
482	0.42	177	249	281	0.073	0.74
467	0.32	170	233	288	0.073	—
575	0.48	139	226	283	0.070	0.50
970	0.35	219	438	528	0.060	0.75
921	0.20	169	439	571	0.046	0.75
582	0.23	205	263	338	0.043	—
231	0.10	111	166	192	0.068	0.69
223	0.05	97	175	201	0.051	0.63
475	0.08	177	272	342	0.045	0.58
468	0.10	256	289	372	0.085	0.41
199	0.24	169	123	142	0.074	0.38
179	0.09	83	138	156	0.103	0.39
205	0.26	93	124	148	0.121	0.70
210	0.48	77	105	129	0.168	0.81
255	0.61	108	110	136	0.172	0.74
218	0.35	77	115	143	0.133	0.73
193	0.23	100	127	144	0.079	0.92
357	0.27	144	211	245	0.068	0.91
592	0.17	120	291	391	0.057	—
160	0.10	99	126	140	0.072	0.92
326	0.41	92	148	174	0.064	0.86
535	0.40	130	217	275	0.062	—
286	0.01	137	161	210	0.063	0.75
829	0.21	185	387	524	0.065	0.56
535	0.20	180	238	340	0.052	0.88
305	0.13	102	177	218	0.064	0.71
301	0.21	103	164	210	0.062	0.37
448	0.30	131	208	266	0.058	0.43
672	0.10	154	403	522	0.077	0.76
516	0.34	89	210	274	0.080	0.86
857	0.33	99	182	285	0.057	0.38
175	0.34	114	98	126	0.086	0.71
65	0.39	61	41	45	0.573	0.63
87	0.25	46	51	62	0.049	—
370	0.21	97	208	249	0.102	—
282	0.46	57	105	136	0.101	0.22
234	0.14	48	99	131	0.088	0.19
970	0.61	256	438	571	0.573	0.92
64	0.01	46	40	44	0.043	0.22
404	0.26	126	200	252	0.091	0.66
357	0.25	113	182	245	0.070	0.71

derived by dividing the corrected σ_D by $\langle D \rangle$. Values of σ_D (uncorrected and corrected), $\langle D \rangle$, and the dispersions (corrected and uncorrected) were produced for each second of the in-cloud measurements.

b. Droplet spectrum geometric standard deviation

Because our droplet concentration retrievals apply a constant geometric standard deviation of droplet size σ_g, we analyze that property here. Values of σ_g were derived from measured spectra by applying a formula in TSI (2012, their second equation). In Fig. 3, we present

the overall ensemble (36 in-cloud segments). The average is $\langle \sigma_g \rangle = 1.4$, and we see that $1.1 < \sigma_g < 1.6$ encompasses most of the range, consistent with the findings of Gerber (1996). None of the σ_g values presented in this study were corrected for instrumental broadening; however, in our analysis of error associated with the lidar-retrieved concentrations, we do evaluate the effect of geometric standard deviations in the range $1.05 \leq \sigma_g \leq 1.60$. As we discuss below, output from our parcel model, evaluated at 85 m above cloud base, is consistent with the low end of this range.
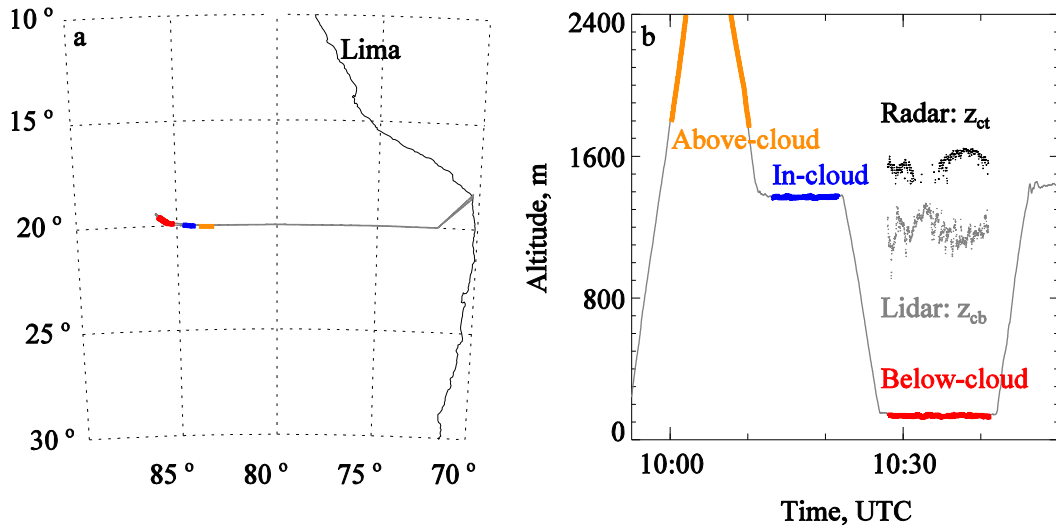
FIG. 1. (a) Sampling segments (above cloud, in cloud, and below cloud) for the example analysis interval. (b) Aircraft altitude during the sampling segments, cloud-base altitude from the upward-pointing lidar (below-cloud segment), and cloud-top altitude from the upward-pointing radar (below-cloud segment).

c. Vertical velocity

The example below-cloud and in-cloud vertical velocity series and the vertical velocity PDFs are plotted in Figs. 4a–c. While it is apparent that the in-cloud PDF is broader (Fig. 4c), this broadening is more evident for downdrafts ($w < 0$). It is the updraft portion of the PDF(w) that is used to derive $\langle N_{\mathrm{mod}} \rangle$ in the parcel model (section 6). Since the altitude of the below-cloud and in-cloud updraft measurements was different from that at cloud base (Fig. 1b), neither measurement is entirely representative of conditions where activation occurs. Values of $\langle N_{\mathrm{mod}} \rangle$ derived using the in-cloud PDF(w) are 6% larger ($\pm 13\%$, segment count = 36) compared to the values of $\langle N_{\mathrm{mod}} \rangle$ based on the below-cloud PDF(w). In

light of this relatively small difference, we elected to use the below-cloud PDF(w) to initialize the parcel model.

Below-cloud averaging times, below-cloud-averaged vertical velocities $\langle w \rangle$, and w standard deviations σ_w are presented in Table 2. Our median σ_w (0.40 m s^{-1}) is consistent with previous measurements made below marine stratocumulus clouds (Guibert et al. 2003; Hudson and Nobel 2014). It is also evident that σ_w is large compared to the magnitude of $\langle w \rangle$.

d. CCN activation spectra

In this section, we describe how measurements from the CCN and PCASP were combined with aerosol hygroscopicity measurements and how these were used to derive
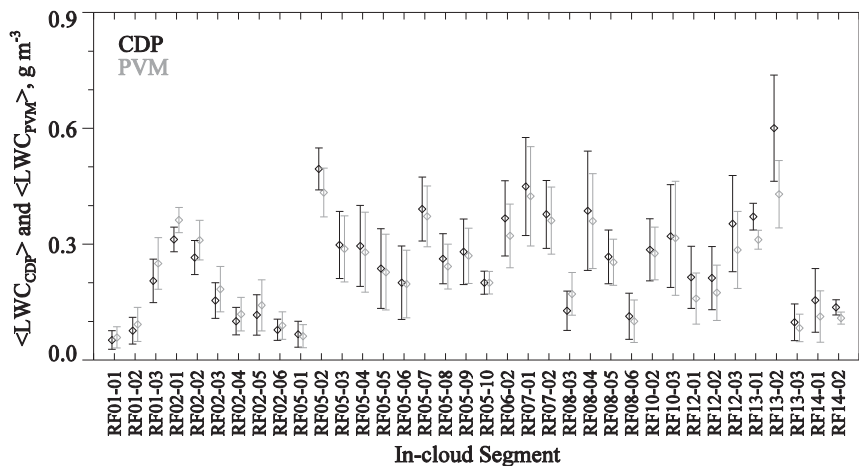

FIG. 2. Averaged CDP and PVM liquid water contents. The abscissa shows the 36 in-cloud segments in chronological order. Error bars are ± 1 std dev.
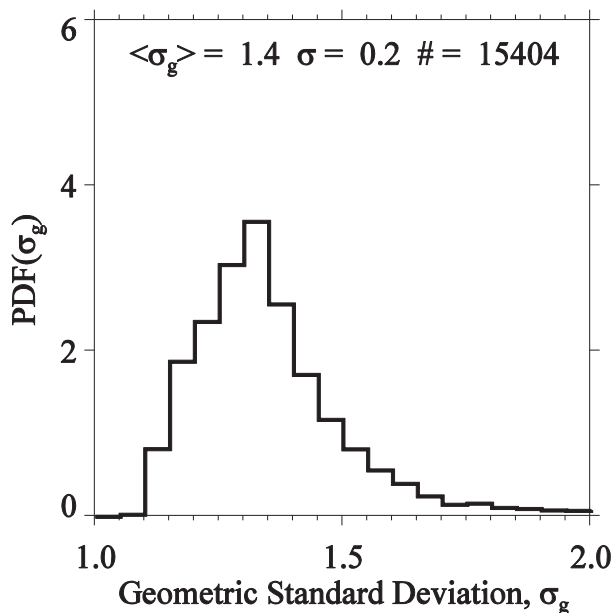
FIG. 3. PDF of σ_g based on 1-s measurements from 36 in-cloud segments. Properties of the data ensemble (average, standard deviation, and number of values) are presented in the legend.

CCN activation spectra. The spectrum from the example below-cloud segment is shown in Figs. 5a and 5b. Our formulation of aerosol hygroscopicity, applied both in appendix A and in the parcel model, is described using the kappa–Köhler formula of Petters and Kreidenweis [2007, their Eq. (11)]. Consistent with results shown in appendix A (see Fig. A2b), the value $\kappa = 0.74$ was accepted as the project average and was used in the parcel model to describe the Köhler curves of particles with dry diameters greater than $0.11\,\mu$m. These are the particles sized and counted by the PCASP (Table A1). For smaller particles we assume the value $\kappa = 0.37$. This is consistent

with a source of CCN coming from downward mixing across the boundary layer inversion and with the fact that a subset of the free-tropospheric particles—those with critical supersaturations larger than 0.3%—are characterized by $\kappa < 0.5$ (Wood et al. 2012, their Fig. 1a). Köhler theory (with the PCASP sizing provided in Table A1) reveals that the range of critical SS accessed by the PCASP (assuming $\kappa = 0.74$) is between 0.001% and 0.11%.

Those portions of the example spectrum derived from the PCASP (SS $<$ 0.11%), and the CCN (SS $>$ 0.11%), are delineated in Fig. 5a. We evaluated the SS $>$ 0.11% portion of the spectrum in two steps. First, we fitted the Wyoming CCN measurements to a function of the form $n(\mathrm{SS}) = C \times \mathrm{SS}^k$ (Fig. 5b), and, second, we discretized the $n(\mathrm{SS})$ function into 40 critical SS classes. The latter are discernible as "steps" in the upper right of Fig. 5a. The fitted values of C and k are presented in Fig. 5b for the example and for each of the 36 analysis intervals in Table 2. The spectrum at SS $<$ 0.11% is based on the below-cloud PCASP measurements, the PCASP size calibration (appendix A), and the kappa-Köhler formula with $\kappa = 0.74$. The lower-left portion of Fig. 5a shows the 30 critical SS classes derived using the 30 size channels of the PCASP (Table A1).

Activation spectra from the PCASP and CCN measurements made during the below-cloud segment and droplet concentrations from the companion in-cloud segments $\langle N_{obs} \rangle$ (Table 2) were used to derive effective supersaturations (SS$_{eff}$; Hudson 1984). Assuming that drizzle and entrainment do not affect $\langle N_{obs} \rangle$, SS$_{eff}$ represents the maximum supersaturation reached within a representative cloud updraft. Eight of our SS$_{eff}$ values are larger than 0.1% (Table 2), and at these supersaturations the spectral slope is smaller than at SS $<$ 0.1% (Fig. 5a; also see Hudson and Nobel 2014). An implication of this is discussed in section 7e.
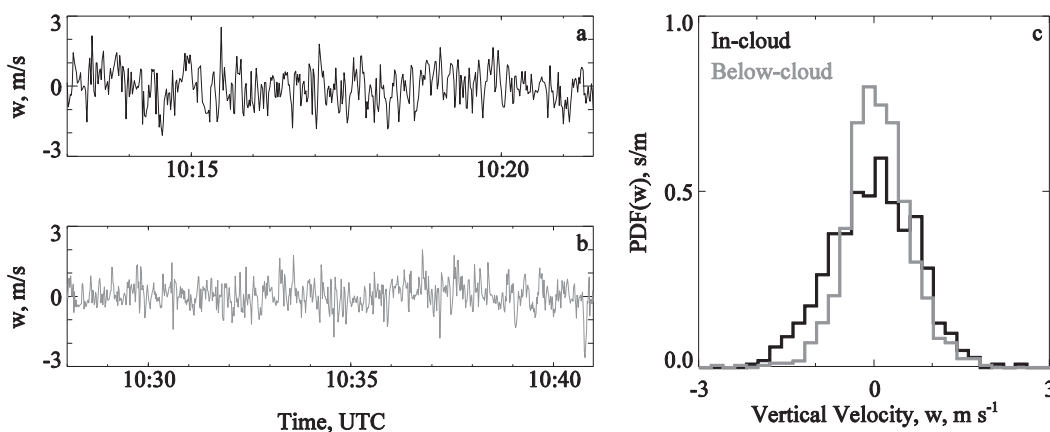

FIG. 4. (a) The example in-cloud vertical velocity sequence, (b) example below-cloud vertical velocity sequence, and (c) the in-cloud and below-cloud vertical velocity PDFs.
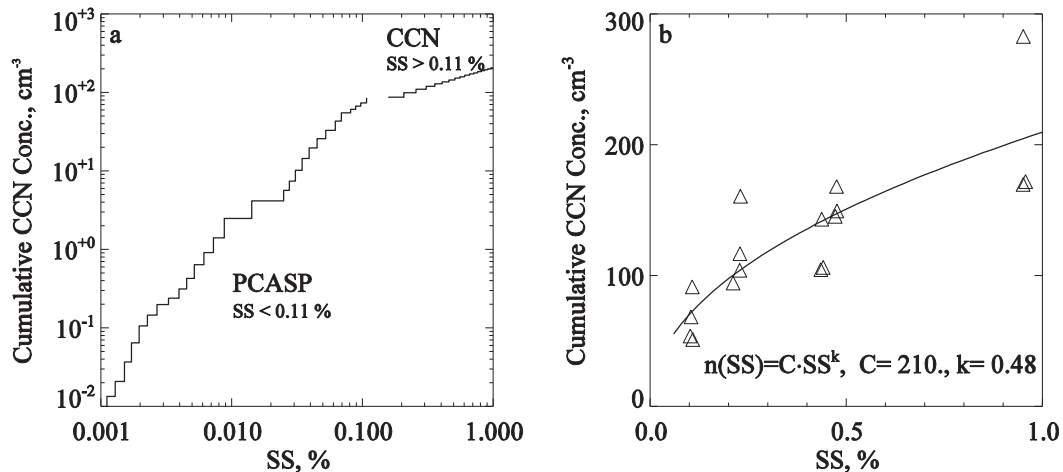
FIG. 5. (a) Activation spectrum for the example interval (RF05; 1028–1041 UTC) with PCASP-derived concentrations (SS < 0.11%) and Wyoming CCN concentrations (SS > 0.11%). (b) CCN measurements from the Wyoming instrument and fit line of form $n(SS) = C \times SS^k$ from the RF05 example interval (1028–1041 UTC). See section 4d for details.

Our median SS_{eff} (0.07%; Table 2) is bracketed by the set of median values reported by Yum and Hudson (2002) for the FIRE and ASTEX field experiments. The FIRE and ASTEX measurements were made over summertime subtropical oceans, and the authors divided the ASTEX measurements into periods affected by maritime and continental air masses. Median SS_{eff} values in Yum and Hudson (2002) are 0.08% (FIRE), 0.31% (ASTEX maritime), and 0.04% (ASTEX continental). Section 7b further describes the continental influence evident in our analysis of the VOCALS CCN and droplet measurements.

5. Vertical profiling measurements and retrievals

Figures 6a–c present remotely sensed cloud properties acquired during the example below-cloud segment. For a cloud forming within a well-mixed boundary layer, variations in z_{cb} should be opposite variations in T_{cb}. This is seen in Figs. 6a and 6b. Furthermore, Fig. 6b shows that RSTT and the lidar-retrieved T_{cb} correlate but also shows that there are portions of the two sequences where the correlation is obscured. This occurs because RSTT's determination of T_{cb} is affected by decreased downwelling longwave flux during periods of thin or broken cloud (e.g., at 1033:30 UTC) and because of the relatively slow response of the RSTT compared to the lidar-retrieved T_{cb} (section 2). With the exception of the three RSTT minima and the lidar's detection of low cloud (scud) at 1028:30 UTC, the temperature sequence reveals a cold shift of the lidar-retrieved T_{cb} relative to RSTT (cold shift $\equiv$ RSST $- T_{cb}$). The cold shift varies between 0° and 2°C.

We also analyzed measurements acquired during climbs executed following the below-cloud segments. For the climb subsequent to the segment shown in Fig. 1b, the vertical θ increase is $+0.2 \text{ K km}^{-1}$. For the 36 climbs, one corresponding to each of the analysis intervals, the median θ increase is $+0.4 \text{ K km}^{-1}$. Therefore, we can say that a fraction of the cold shift is due to thermodynamic stability within the subcloud layer. The rest of the cold shift is likely due to positive bias in RSTT, possibly due to radiation from water vapor in the intervening subcloud layer. We do not investigate the suspected bias in RSTT, but we do evaluate uncertainty in T_{cb}, due to either measurement error or to departure from the well-mixed assumption (section 2), and account for how that error propagates into the retrieval (section 5d).

a. Lidar-retrieved extinction profile and cloud base

Our retrieval of N begins with the lidar measurement of a vertical profile of the attenuated backscatter. The analysis has two steps: 1) inversion of the profile of attenuated backscatter to determine the profile of the extinction coefficient (Klett 1981) and 2) determination of N. In the first step, the extinction-to-backscatter ratio is set to the value expected for a population of cloud droplets (O'Connor et al. 2004). In addition, the inversion uses an estimate of the extinction coefficient β at a point in the cloud that produces diminished, but not negligible, returned power. This particular β defines an upper boundary condition (Klett 1981). The inversion also uses a relationship between the lidar-measured depolarization (Z. Wang et al. 2009) and multiple scattering (Hu et al. 2007) and applies this to correct for the effect of multiple scattering on the attenuated
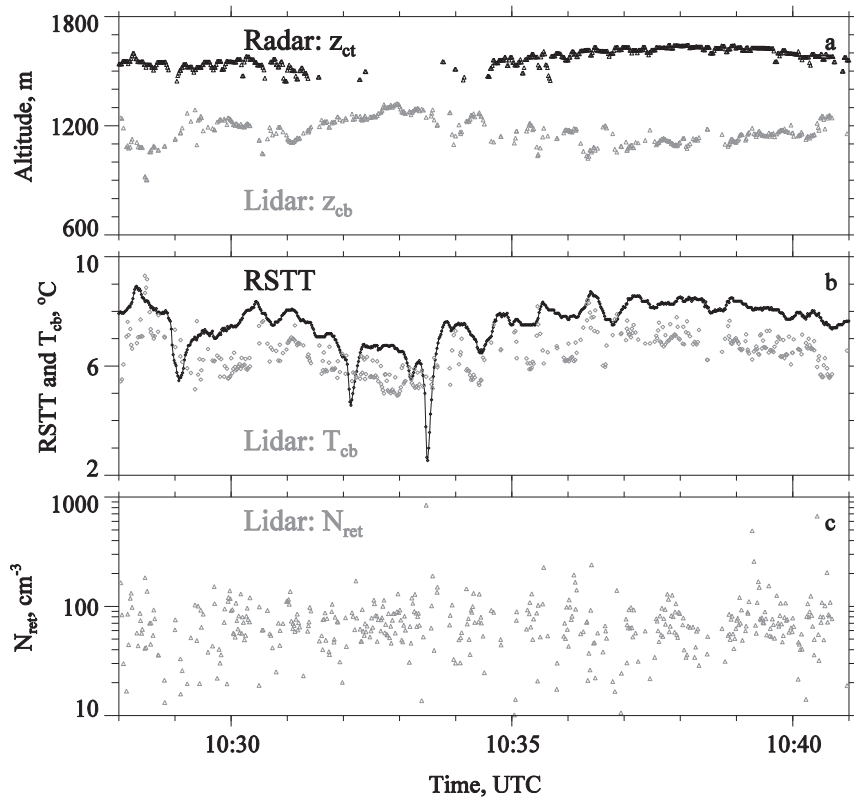
FIG. 6. Properties retrieved by remote sensors during the example below-cloud sequence (RF05; 1028–1041 UTC). (a) Radar-retrieved z_{ct} and lidar-retrieved z_{cb}. (b) Upward-viewing radiative temperature from RSTT and lidar-retrieved T_{cb}. (c) Lidar-retrieved droplet concentration N_{ret}. All properties were resampled at 1 Hz for plotting clarity. See text for details.

backscatter and therefore on the extinction coefficient. Once the extinction profile is evaluated, z_{cb} can be retrieved; the basis for this is described in Platt et al. (1994) and Wang and Sassen (2001).

b. Droplet concentration retrieval

The focus of the second step (section 5a) is a layer extending upward from 20 m above z_{cb}. For this layer, we evaluated many theoretical extinction profiles, compared these to the lidar-retrieved extinction profile, and from these comparisons inferred N. The theoretical extinction profiles are dependent on two assumptions: 1) the LWC profile is described by an adiabatic model, and 2) the droplet spectrum is a lognormal with constant N and constant geometric standard deviation ($\sigma_g = 1.4$; section 4b). Because of the first assumption, we refer to any one of the theoretical extinction profiles as an "adiabatic extinction."

The equation we use to describe the profile of adiabatic LWC is

$$\text{LWC}(z) = \Gamma \times (z - z_{cb}), \quad z_{cb} \le z \le z_{ct}, \quad (1)$$

where z is altitude and Γ is an adiabatic LWC lapse rate.[2] Adiabatic extinctions were evaluated by varying two properties: 1) T_{cb} (varied within ± 0.5 K of the lidar-retrieved T_{cb}), and 2) z_{cb} (varied within ± 20 m of the lidar-retrieved z_{cb}). In each variation step, N was evaluated by applying the constraints of adiabatic LWC and measured extinction at a prescribed height above cloud base.

Another equation [Frisch et al. (1995), their Eq. (2)] was used to relate N, σ_g, and the lognormal's geometric mean diameter D_g (TSI 2012) to an extinction:

$$\beta = (\pi/2)ND_g^2 e^{2(\ln\sigma_g)^2}. \quad (2)$$

Because LWC is a function of altitude [Eq. (1)], both D_g and the adiabatic extinction coefficient β [Eq. (2)] are altitude dependent.

----

[2] Evaluated using Eq. (1) in Albrecht et al. (1990), multiplied by the density of air. The temperature- and pressure-dependent Γ was evaluated at a state defined by the lidar-retrieved values T_{cb} and P_{cb}.
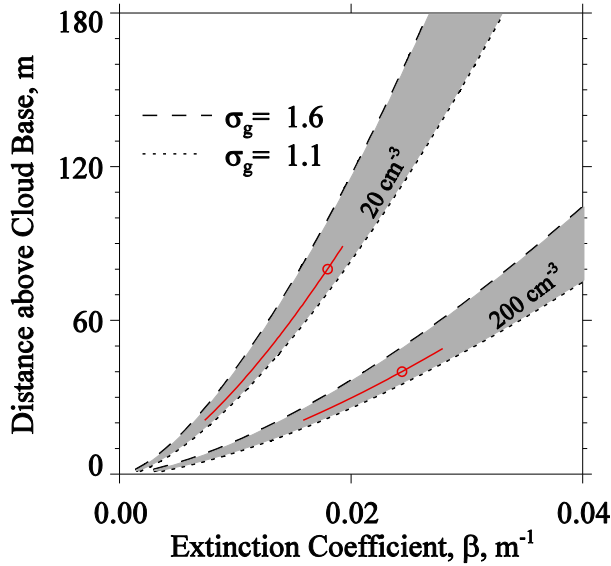
FIG. 7. Relationship between distance above cloud base and extinction coefficient for different values of N and σ_g. The gray regions are defined by $N = 20$ and $200 \, \text{cm}^{-3}$. The left and right boundaries of these regions are at $\sigma_g = 1.6$ and 1.1, respectively. The left and right red curves, are extinction profiles derived with $N_o = 22.5 \, \text{cm}^{-3}$ and $\sigma_{g,o} = 1.40$ and $N_o = 225 \, \text{cm}^{-3}$ and $\sigma_{g,o} = 1.40$, respectively; they intersect hypothetical lidar-retrieved states (red circles) that can also be matched by $N = 20.0 \, \text{cm}^{-3}$ and $\sigma_g = 1.31$ and $N = 200 \, \text{cm}^{-3}$ and $\sigma_g = 1.31$, respectively.

The lidar-retrieved β profile was compared to the adiabatic profiles over a range that extended from $z_{cb} + 20 \, \text{m}$ to approximately $z_{cb} + 150 \, \text{m}$, and a relative error statistic was formulated for each of the comparisons:

$$\text{RE} = \frac{1}{n} \left[\frac{(\beta_{i,\ell} - \beta_i)^2}{\beta_{i,\ell}^2} \right]. \qquad (3)$$

Here, n is the number of lidar range gates within a profile, $\beta_{i,\ell}$ is an element of the lidar-retrieved extinction profile, and β_i is an element of an adiabatic profile. The N associated with the set $\{T_{cb,j}, z_{cb,j}\}$ that minimizes RE was set equal to the retrieved cloud droplet concentration N_{ret}. Averaged retrieved concentrations are presented in Table 2.

Figure 7 illustrates the adiabatic calculation for idealized clouds with the same LWC lapse rate ($2 \, \text{g m}^{-3} \, \text{km}^{-1}$) and two values of N and σ_g. The basis for the retrieval is the sensitivity of the extinction to N. Also evident is sensitivity to σ_g, with larger values corresponding to smaller extinctions and vice versa. We quantify the N–σ_g and N–Γ sensitivities in section 5d.

Gaps are evident in the lidar-retrieved quantities seen in Figs. 6a–c (i.e., z_{cb}, T_{cb}, and N_{ret}). The gap at ~1038:30 UTC results because we discarded lidar retrievals associated with RE > 0.01 [Eq. (3)]. Although not relevant to the

sequence in Fig. 6, some of the below-cloud segments also have retrievals coincident with an RSTT < −20°C. These portions of the RSTT time series were interpreted as breaks in the cloud and were also discarded. Gaps in the radar sequence (i.e., between 1031:30 and 1034:30 UTC in Fig. 6a) are also evident. These result because the radar reflectivity was less than the minimum detectable by the upward-pointing beam of the Wyoming Cloud Radar (−20 dBZ at 1 km).

c. Assumptions

Using measurements from the in-cloud portions of the climbs (section 5), we now examine the adiabatic LWC, constant-N, and $\sigma_g = 1.4$ assumptions made in the previous section. Measurements from the climb that followed the example interval (Fig. 1b) are shown in Fig. 8. Figure 8a has LWC measurements normalized by adiabatic LWCs, Fig. 8b has concentrations normalized by the climb average, and Fig. 8c has σ_g. These profiles are represented by red triangles. Shown in gray are the same properties averaged over 25 climbs (gray triangles ± 1 std dev). This count is smaller than the total number of climbs (36) because 11 passed through a break in the cloud, ended at an altitude less than 150 m above cloud base, or encountered cloud thinner than 150 m. The averaged profiles confirm the three assumptions; however, in Fig. 8a the example departs significantly from the adiabatic LWC profile. A reason for this could be variation in cloud-base height during the climb. In Fig. 6a, there is evidence for this and for the fact that substantial cloud-base height variations (>100 m) often occur on a scale comparable to the time for the 150-m climbs (~35 s). In the lower 100 m of the σ_g profile (Fig. 8c), the CDP measurements (red triangles) trend in a manner consistent with the prediction of our parcel model (not shown). Above 120 m, σ_g is increased, and this occurs in association with LWC subadiabaticity and decreased $N/\langle N \rangle$. This indicates that entrainment, in addition to adiabatic processing, likely also affected σ_g within the lower portion of the cloud layer sensed by the lidar.

d. Error analysis

As we described in section 5b, adiabatic profiles of LWC and β, and a lidar-retrieved β profile, are the elements we use to retrieve N_{ret}. A component of the calculation is the temperature- and pressure-dependent value of Γ [Eq. (1)]. For the following error analysis, we fix P_{cb} at a value representative of the southeast Pacific stratocumulus (900 hPa). This is justified because Γ is more sensitive to T_{cb}, compared to P_{cb} (Table 3). With P_{cb} approximated as a constant, we now demonstrate how shifts in T_{cb} and σ_g affect N_{ret}. For these objectives, we adopt the following equation [Young (1962), their Eq. (2.9)]:
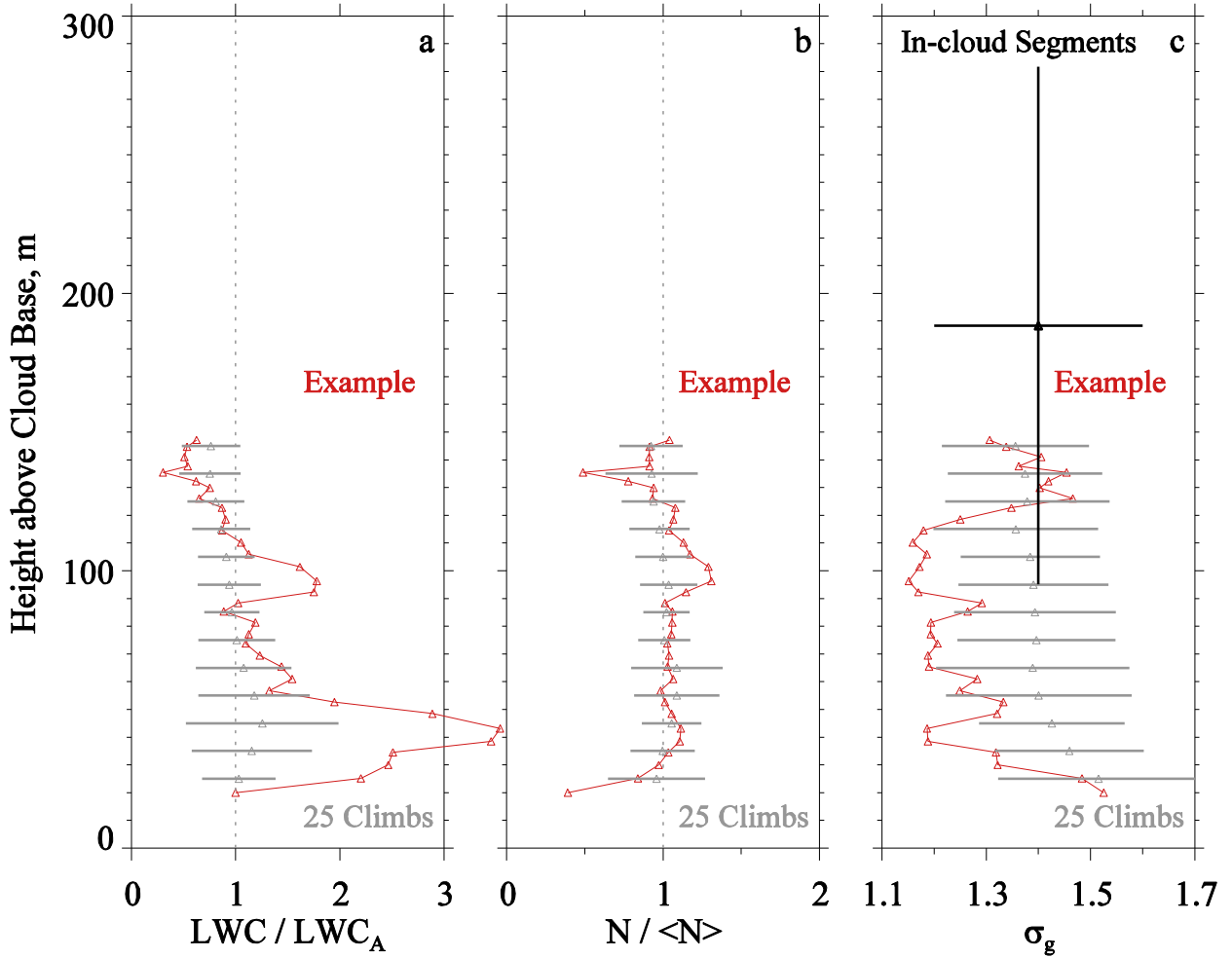
FIG. 8. Cloud properties between cloud base + 20 m and cloud base + 150 m from the climb following the example below-cloud segment (red triangles; 1-s CDP measurements) and the same properties averaged over the 25 climbs (gray triangles ± 1 std dev). (a) Measured LWC divided by the adiabatic LWC. (b) Measured concentration divided by the 20–150-m average. (c) Measured σ_g. Figure 8c also shows the averaged σ_g, from measurements made during the in-cloud segments (section 4b) and plotted at the average height of in-cloud segments (black triangle ± 1 std dev).

$$\frac{N - N_o}{N_o} = (\Gamma - \Gamma_o) \left(\frac{1}{N} \frac{\partial N}{\partial \Gamma} \right)_{\Gamma_o, \sigma_{g,o}}$$

$$+ (\sigma_g - \sigma_{g,o}) \left(\frac{1}{N} \frac{\partial N}{\partial \sigma_g} \right)_{\Gamma_o, \sigma_{g,o}}, \qquad (4a)$$

$$\left(\frac{1}{N} \frac{\partial N}{\partial \Gamma} \right)_{\Gamma_o, \sigma_{g,o}} = \frac{-2}{\Gamma_o} \quad \text{and} \qquad (4b)$$

$$\left(\frac{1}{N} \frac{\partial N}{\partial \sigma_g} \right)_{\Gamma_o, \sigma_{g,o}} = \frac{6 \ln(\sigma_{g,o})}{\sigma_{g,o}}. \qquad (4c)$$

where N is a perturbed concentration, and N_o is the concentration retrieved using default settings (i.e., $\sigma_{g,o} = 1.4$ and Γ_o evaluated using the lidar-retrieved T_{cb}). The normalized derivatives in Eq. (4a) are useful for quantifying how the concentration is altered when the geometric standard deviation is shifted from $\sigma_{g,o}$ or Γ is shifted from Γ_o. The two derivatives were evaluated analytically, and we confirmed those findings numerically. The result is

First, we investigate the lidar-retrieved values of T_{cb}, their shift from RSTT (Fig. 6b), and how that shift

TABLE 3. Sensitivity of Γ to cloud-base temperature and pressure.

	$P_{cb} = 900$ hPa	$P_{cb} = 950$ hPa
$T_{cb} = 5°C$	$\Gamma = 1.86$ g m^{-3} km^{-1}[a]	$\Gamma = 1.92$ g m^{-3} km^{-1}
$T_{cb} = 10°C$	$\Gamma = 2.10$ g m^{-3} km^{-1}	$\Gamma = 2.16$ g m^{-3} km^{-1}

[a] Evaluated using Eq. (1) in Albrecht et al. (1990), multiplied by the density of air.
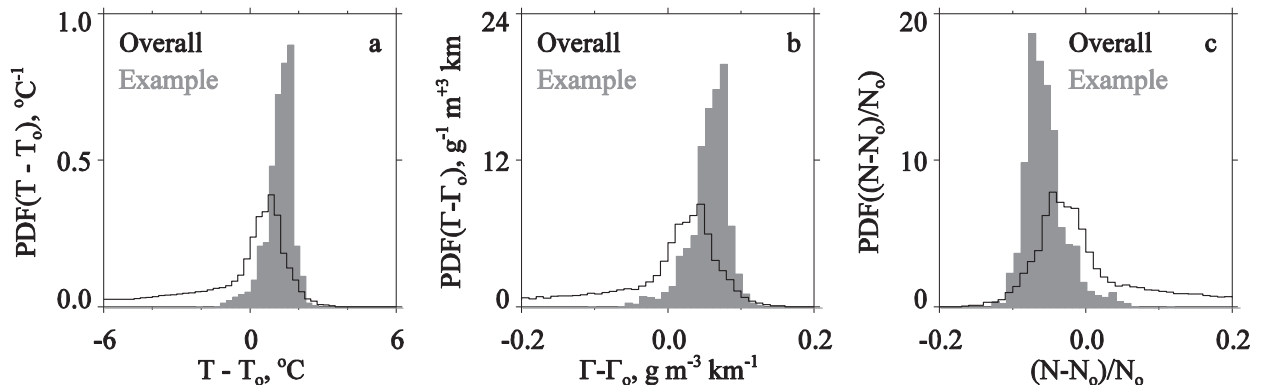
FIG. 9. (a) Distribution of temperature difference based on cloud-base temperatures from the lidar ($T_o = T_{cb}$) and from the upward-viewing radiometric temperature sensor (T = RSTT). The "Example" is the 1028–1041 UTC below-cloud segment from RF05. Values from the 36 analysis intervals are represented in the "Overall" distribution. (b) Distribution of LWC lapse-rate difference (P_{cb} is set equal to 900 hPa). (c) Distribution of the relative error in retrieved N using Eq. (4a) (with the σ_g derivative set to zero), Eq. (4b), and the distributions in Fig. 9b.

affects the retrieved N. In this analysis, we indicate the default setting with subscript o (i.e., $T_o = T_{cb}$), and we do not subscript the perturbed setting (i.e., T = RSTT). Figure 9a portrays the point-by-point temperature differences as a distribution. The $T - T_o$ values used to construct the gray distribution come from the example below-cloud segment (Fig. 6b). Also shown is the distribution aggregated from the 36 below-cloud segments. We see that the modes of these distributions are at $+1.8°C$ (example) and at $+0.7°C$ (overall). Also evident (Fig. 9a) is a broad left tail in the overall $T - T_o$ distribution; this is due to the radiometric sensor's large underestimation of T_{cb} when it views thin or broken cloud (section 5). Figure 9b has the distribution of $\Gamma - \Gamma_o$. The pattern seen here is consistent with that in Fig. 9a.

Figure 9c shows the distribution of the relative N error. This was derived using Eq. (4a), with the σ_g derivative set to zero, Eq. (4b), and the distributions in Fig. 9b. The modes of these distributions (Fig. 9c) tell us that the cold shift (section 5) translates to an error in N that is -8% (example) and -5% (overall). We note that smaller values of N would have resulted had the generally larger values of RSTT been applied in the retrieval. This makes physical sense because a warmer cloud base means that the adiabatic LWC is increased, and therefore an N value smaller than N_o must be applied to match the adiabatic extinction to the lidar-retrieved extinction.

The question of a systematic σ_g bias is relevant because the σ_g assessment was based on in-cloud measurements made ~200 m above cloud base (Fig. 8c and section 4b). While this altitude was useful for documenting cloud properties, it may have produced a value of $\langle \sigma_g \rangle$ that is unrepresentative of the lower part of the cloud probed by the lidar. Parcel model predictions of the droplet spectrum standard deviation σ_D with ascent upward from cloud base reinforce this suspicion (Rogers and Yau 1989,

their Fig. 7.4). Relative concentration errors, calculated using Eq. (4a), with the Γ derivative set to zero, and using Eq. (4c) are presented in Table 4. The value $\sigma_g = 1.05$ (Table 4) is representative of output from our parcel model evaluated at $z - z_{cb} = 85$ m. We note that in the limit of closed parcel ascent, with $\sigma_g = 1.05$, N is 50% smaller than N_o. The reason for this is that a decreased σ_g means that an N smaller than N_o must be applied to match a lidar-retrieved extinction. An example of this positive N–σ_g correlation is shown graphically in Fig. 7, where two hypothetical lidar-retrieved states (red circles) are matched by red curves. On the left, the red curve is defined by $N_o = 22.5$ cm^{-3} and $\sigma_{g,o} = 1.40$, and this is seen to intersect a state that can also be matched by $N = 20.0$ cm^{-3} and $\sigma_g = 1.31$. On the right, the red curve is defined by $N_o = 225$ cm^{-3} and $\sigma_{g,o} = 1.40$, and this is seen to intersect a state that can also be matched by $N = 200$ cm^{-3} and $\sigma_g = 1.31$.

6. Parcel model concentration

Modeled concentrations were derived using the parcel model described in Snider et al. (2003). A subcomponent of this is the droplet growth equation; for this we used the

TABLE 4. Sensitivity of retrieved concentration to σ_g. The relative concentration error is derived using Eqs. (4a) and (4c) with the Γ derivative set to zero in Eq. (4a). The default geometric standard deviation is $\sigma_{g,o} = 1.4$.

Geometric std dev σ_g	Relative concentration error
1.05	-0.50
1.10	-0.43
1.20	-0.29
1.30	-0.14
1.40	0.00
1.50	$+0.14$
1.60	$+0.29$

formulation of Zou and Fukuta (1999) (Snider et al. 2003), and we applied the value of 1.0 for the efficiency of vapor accommodation on droplets (Davidovits et al. 2004; Laaksonen et al. 2005). Different from Snider et al. (2003), our description of RH over both haze droplets and cloud droplets is in terms of a temperature- and composition-independent formula for the Kelvin effect (Snider et al. 2010) and in terms of a dimensionless parameter known as kappa (κ) for the solute effect (Petters and Kreidenweis 2007).

The model's initial thermodynamic state was evaluated by extrapolating the averaged lidar-retrieved T_{cb} and P_{cb} (section 2), at constant specific humidity and constant specific entropy, to RH = 95% (Iribarne and Godson 1981, chapter 7). Haze particle diameters at RH = 95% were derived using kappa–Köhler theory and using our description of κ (section 4d). The model was also initialized with the below-cloud-averaged CCN activation spectra, but these were first scaled to account for expansion. The scaling factor is the ratio of air density at the initial state divided by the below-cloud segment air density. Vertically decreasing density-corrected concentrations were detected during some of the climbs (section 5), but this was not accounted for. The parcel model was used to evaluate sets of droplet concentration $N(w)$, and droplet spectra, at 200 m above cloud base. The updrafts used in the simulations ranged from 0.05 to 3.0 m s^{-1} in 0.05 m s^{-1} increments. Typically, only the smallest of the 60 possible updrafts need to be modeled; the largest updrafts have negligible statistical weight (e.g., Fig. 4c)

and therefore do not contribute to the statistics we derive.

The average concentration was evaluated as

$$\langle N_{mod} \rangle = \sum N(w_i) \mathrm{PDF}(w_i) \Delta w. \quad (5a)$$

Here, $\mathrm{PDF}(w_i)\Delta w$ is the fraction of updrafts in an interval Δw centered at w_i. Equation (5a) represents the average as a convolution of two opposing effects: 1) the increase of N with updraft and 2) the smaller frequency of occurrence of large updrafts relative to small updrafts (Fig. 4c). We refer to $\langle N_{mod} \rangle$ as an *unweighted* average. In addition, an *updraft-weighted* average was evaluated:

$$\langle N_{mod,w} \rangle = \frac{1}{\sum w_i \mathrm{PDF}(w_i) \Delta w} \sum N(w_i) w_i \mathrm{PDF}(w_i) \Delta w. \quad (5b)$$

Some consideration of the relevance of Eqs. (5a) and (5b) is needed. Equation (5a) is the average expected for sampling of measured concentrations, or model-derived concentrations, within upward-moving air a few tens of meters above cloud base (Meskhidze et al. 2005). Conversely, the numerator of Eq. (5b) can be interpreted as the flux of droplets entering a cloud model grid box. Hence, $\langle N_{mod,w} \rangle$ and a vertical velocity PDF can be used to validate a droplet source function within a model scheme (Ghan et al. 1997; Meskhidze et al. 2005). Concentrations derived using Eqs. (5a) and (5b) are presented in Table 2.

The next two equations define PDF widths corresponding to the unweighted and updraft-weighted concentrations:

$$\sigma_{mod} = \left\{ \sum [N(w_i) - \langle N_{mod} \rangle]^2 \mathrm{PDF}(w_i) \Delta w \right\}^{1/2} \quad \text{and} \quad (5c)$$

$$\sigma_{mod,w} = \left\{ \frac{1}{\sum w_i \mathrm{PDF}(w_i) \Delta w} \sum [N(w_i) - \langle N_{mod,w} \rangle]^2 w_i \mathrm{PDF}(w_i) \Delta w \right\}^{1/2}. \quad (5d)$$

7. Results

a. Concentration probability distribution functions

Averaged concentrations $\langle N_{obs} \rangle$ (section 4a), $\langle N_{ret} \rangle$ (section 5b), $\langle N_{mod} \rangle$, and $\langle N_{mod,w} \rangle$ (section 6) are available for each analysis interval (Table 2). The four PDFs for the example interval are shown in Fig. 10. Values aggregated into these ensembles come from the appropriate segment of the analysis interval; for example, the PDF(N_{obs}) in Fig. 10a was obtained by aggregating measurements from the in-cloud segment. Locations of the in-cloud and below-cloud segments, for the example

interval, are shown in Fig. 1, and the N_{ret} sequence is plotted in Fig. 6c.

The two model-based PDFs (unweighted and updraft weighted) are presented in Fig. 10b. The unweighted PDF was binned into the same regularly spaced categories used for the observed and retrieved values, but the binning used for PDF($N_{mod,w}$) is dependent on the updraft increment (0.05 m s^{-1}; section 6) and is therefore somewhat different. The averages are $\langle N_{ret} \rangle$ = 77 cm^{-3}, $\langle N_{obs} \rangle$ = 90 cm^{-3}, $\langle N_{mod} \rangle$ = 105 cm^{-3}, and $\langle N_{mod,w} \rangle$ = 129 cm^{-3}. The PDF widths are different as well. In Fig. 10b it is evident that updraft weighting
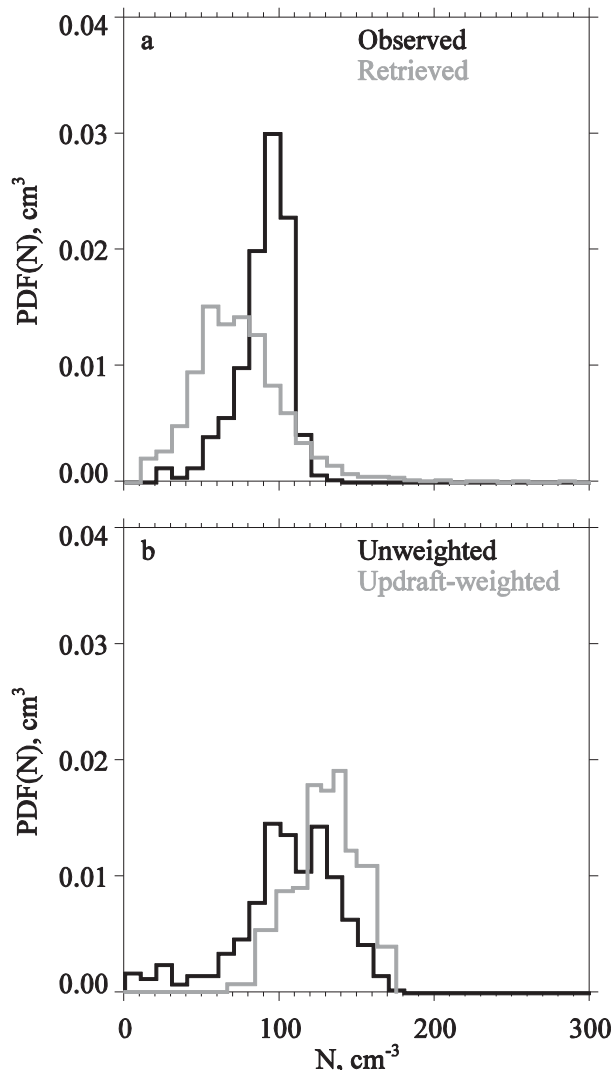
FIG. 10. Concentration PDFs for the example in-cloud segment (RF05; 1013–1021 UTC) and the example below-cloud segment (RF05; 1028–1041 UTC). (a) The observation-based and retrieval-based PDFs. (b) The unweighted model and updraft-weighted model PDFs.

attenuates the left tail of the PDF, making that width the second smallest of the four presented, while in Fig. 10a a larger width is evident for the retrieval-based PDF. The widths are ranked in the following order: observation ($\sigma_{obs} = 17 \, cm^{-3}$), updraft-weighted model ($\sigma_{mod,w} = 23 \, cm^{-3}$), unweighted model ($\sigma_{mod} = 33 \, cm^{-3}$), and retrieval ($\sigma_{ret} = 50 \, cm^{-3}$).

b. Longitudinal dependence

Systematic variation of droplet concentration within the southeast Pacific stratocumulus sheet is documented in published analyses of the VOCALS dataset and in work that preceded the campaign. Figure 11

shows a longitudinal concentration gradient with smaller values away from the coast. This is consistent with the southerly low-level airflow along the Chilean coast at midlatitudes, the continental aerosol contained in that flow, and the aerosol removal that occurs as the flow turns out to sea in the subtropics (Kuang and Yung 2000; Leon et al. 2008; Wood et al. 2008; Hawkins et al. 2010; Wood et al. 2012; Twohy et al. 2013). In addition, a comparison of Figs. 11a and 11b establishes that retrieval-based averages are, with some exceptions, smaller than observation-based averages. It is also generally true that $\langle N_{obs} \rangle < \langle N_{mod} \rangle$ and that $\langle N_{obs} \rangle < \langle N_{mod,w} \rangle$ (Table 2).

c. Decoupling

Within a stratocumulus-topped boundary layer it is common for a thermodynamically defined lifted condensation level (LCL) to occur a few hundred meters below a lidar-retrieved cloud base (Bohren and Albrecht 1998, their Fig. 6.1). In general, two processes are responsible for this: 1) entrainment of above-cloud air into the boundary layer and 2) the downward flux of condensate carried by drizzle (Jones et al. 2011). The concept here is that entrainment and drizzle tend to increase cloud-base height; this is counter to the common assumption that entrainment and drizzle result in subadiabatic LWC but not necessarily an increased z_{cb}. In what follows, we interpret the decoupling microphysically and derive a correction factor that we subsequently apply in the concentration comparisons. This amounts to the assumption that parcels entered the cloud at the LCL and were subsequently modified with the N reduction following the reduction in LWC.

The basis for the correction is our two independent assessments of cloud-base altitude. Consider the example below-cloud segment and the lidar's measurement of z_{cb} during that segment (Fig. 6a). When combined with a radar-retrieved cloud-top altitude, a cloud thickness H_1 can be derived. Also, the lidar-retrieved z_{cb}, combined with C-130 measurements of temperature, pressure and altitude, can be used to derive an adiabatic LWC lapse rate Γ_1. Alternatively, C-130 measurements of dewpoint (section 2), temperature, and pressure can be used to derive an LCL and the adiabatic LWC lapse rate at the LCL Γ_2. When the LCL information is combined with the radar-retrieved cloud-top altitude, a second cloud thickness H_2 can also be derived.

We interpret the microphysical impact of entrainment and drizzle in the following way. First, using definitions made in the previous paragraph we denote a lidar-retrieved and a thermodynamically derived value
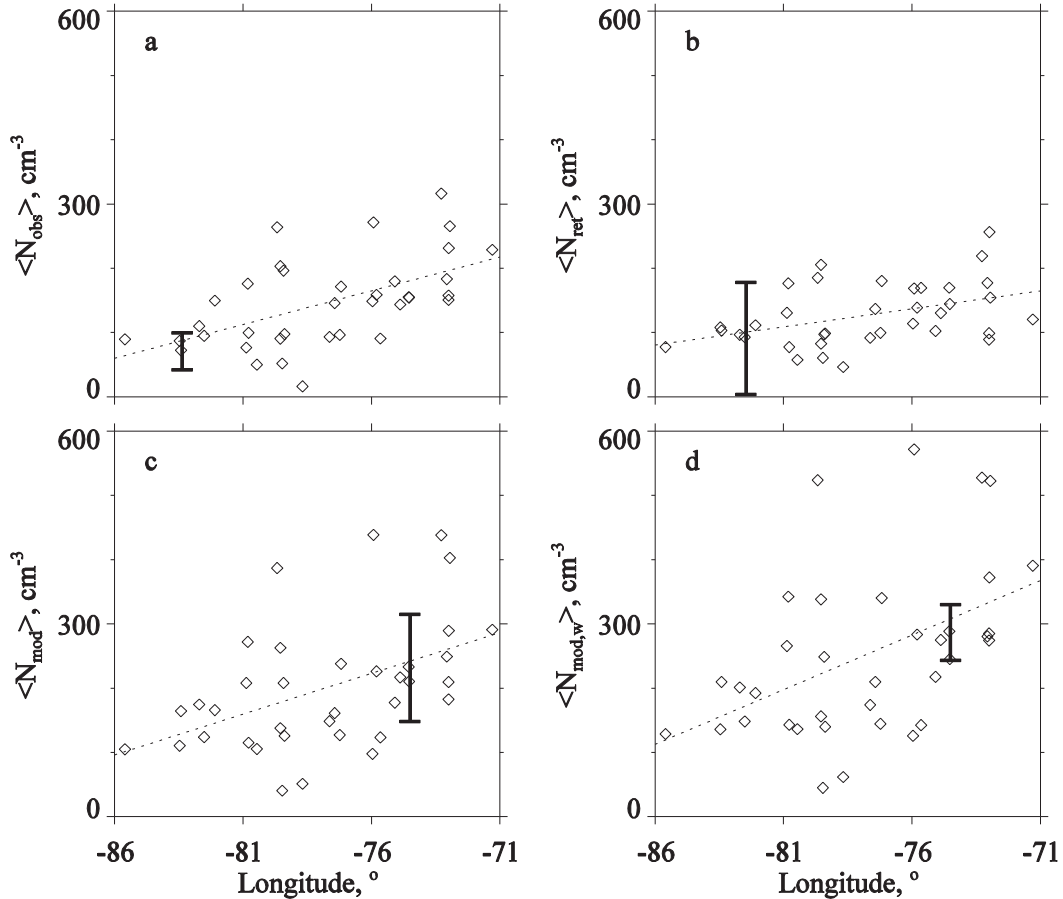
FIG. 11. (a) Observed cloud droplet concentration $\langle N_{obs}\rangle$ vs longitude and the fit line. (b) As in (a), but for the retrieved concentration $\langle N_{ret}\rangle$. (c) As in (a), but for the unweighted model concentration $\langle N_{mod}\rangle$. (d) As in (a), but for the updraft-weighted model concentration $\langle N_{mod,w}\rangle$. In all panels, a ± 1 PDF width interval is drawn on the average associated with the median PDF width.

of cloud-top LWC as $\Gamma_1 H_1$ and $\Gamma_2 H_2$, respectively. Then we calculate the ratio these LWC values and equate the ratio to a factor we define as the correction factor:

$$CF = \frac{\Gamma_1 H_1}{\Gamma_2 H_2} = \frac{N}{N_A}. \tag{6}$$

In Eq. (6), we see the droplet concentration N resulting from a combination of processes (activation, entrainment, and drizzle) and the adiabatic value solely due to activation N_A. Implicit in Eq. (6) is the assumption that entrainment and drizzle diminish droplet concentration in proportion to their diminishment of LWC.

Averaged values of the CF were derived for 30 of the 36 below-cloud segments. The reason for missing averages is that z_{ct} was not available because the radar reflectivity was less than the minimum detectable (section 5b) during

six below-cloud segments. The below-cloud averaged CF values range from 0.2 to 0.9 ($\bar{x} = 0.7 \pm 0.2$, segment count = 30) and are thus constrained between 0 and 1 in a manner consistent with the definition provided in Eq. (6). Also, two characteristics of the CF are evident. In general, the CF was relatively large (CF $\sim$ 1) in regions where the lidar and radar profiles show cumulus penetrating into stratocumulus, and it was relatively small in some regions with higher-based stratocumulus. Examples of both cloud types are evident in Zuidema et al. (2012, their Fig. 8).

Figure 12 demonstrates that the modeled concentrations are approximately 30% larger than the observed values (black circles and black fit line of form $Y = aX$). The figure also shows that CF decreases the modeled values (red circles) and that this decrease makes the second fit line (red) statistically indistinguishable from unity, indicating agreement between the CF-adjusted model (CF $\times \langle N_{mod}\rangle$) and observations $\langle N_{obs}\rangle$. Our
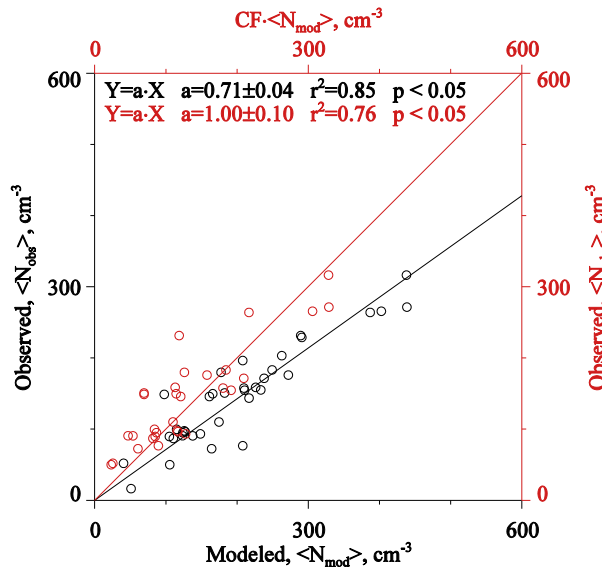
FIG. 12. Black circles are the observed/modeled concentration pairs (segment count = 36), and red circles are observed/modeled concentration pairs with the latter adjusted by the correction factor (CF; segment count = 30). The y deviations are the basis for the least squares criterion of best fit (Young 1962). The confidence interval on the fitted coefficient was derived using Student's t distribution at the 95% level (Havlicek and Crain 1988). The significance of the Pearson correlation coefficient r was evaluated in a two-tailed test using Student's t distribution at the 95% level (Havlicek and Crain 1988).

statistical inference holds true regardless of whether vertical or horizontal deviations between the points and the fit line (i.e., the y and x deviations, respectively) are used to evaluate the confidence interval on the fitted coefficient (Havlicek and Crain 1988). In a regression of the retrieved concentrations $\langle N_{ret} \rangle$ plotted versus corrected model concentrations (CF $\times$ $\langle N_{mod} \rangle$) the fitted coefficient is also indistinguishable from unity (not shown); however, this is only true when x deviations are used to evaluate the confidence interval on the fitted coefficient. More variability is also apparent in the plot of $\langle N_{ret} \rangle$ versus CF $\times$ $\langle N_{mod} \rangle$ (not shown); this is consistent with the fact that the square of the Pearson correlation coefficient ($r^2 = 0.48$) for the $\langle N_{ret} \rangle$ versus CF $\times$ $\langle N_{mod} \rangle$ regression is smaller than the correlation coefficient ($r^2 = 0.76$) in Fig. 12.

d. Cloud droplet concentration variability

Rather than indicate the concentration variability associated with each point, in Fig. 11 we draw a plus or minus one PDF width interval on the average associated with the median PDF width. The result for these four widths is representative of what we discussed in section 7a and is consistent with our overall finding: variability on $\langle N_{mod} \rangle$ is larger than on $\langle N_{obs} \rangle$, variability on $\langle N_{mod,w} \rangle$

is intermediate between that on $\langle N_{obs} \rangle$ and $\langle N_{mod} \rangle$, and variability on $\langle N_{ret} \rangle$ is largest.

e. Spectral dispersion

Here we compute a spectrum by mixing individual spectra generated for each of the modeled updrafts. We also compute an N, σ_D, $\langle D \rangle$, and a dispersion corresponding to the mixture spectrum. The mixture spectrum is broadened relative to the individual spectra because the latter are characterized by a range of N, as a result of activation as a function of updraft, and because of the resultant variation of $\langle D \rangle$ at the height where the individual spectra are evaluated (200 m above cloud base). Implicit in our analysis are two hypotheses: 1) PDF(w_i)Δw describes the fractional contribution of individual spectra to the mixture [Eq. (5a)] and 2) mixing produces a locally homogeneous concentration. Our hypotheses are linked to two processes: 1) differential activation at cloud base (Stevens et al. 1996) and 2) mixing without entrainment (internal mixing; Hudson and Svensson 1995).

Values of σ_D and $\langle D \rangle$, derived for the mixture spectrum, were analyzed with the values of σ_{mod} and $\langle N_{mod} \rangle$ described previously (section 6). The following theoretical relationship, developed by Cooper (1989), relates these statistics:

$$\frac{\sigma_D}{\langle D \rangle} = \frac{1}{3} \frac{\sigma_{mod}}{\langle N_{mod} \rangle}. \quad (7)$$

Figure 13 shows a scatterplot of modeled spectral dispersions and modeled concentration dispersions. The slope of the fit line is nearly equal to one-third. Hence, we conclude that Cooper's theory and our modeling are consistent. Because Cooper developed his theory with the same assumption that parcels experience closed-parcel adiabatic ascent prior to internal mixing, and that is also implicit in our calculations, this consistency is expected. The consistency evident in Fig. 13 is important because it demonstrates that σ_{mod}, $\langle N_{mod} \rangle$, and Eq. (7) can be used to derive a spectral dispersion for parcels that follow varied updrafts and subsequently mix. We also note that σ_{mod} and $\langle N_{mod} \rangle$ can be derived with knowledge of PDF(w) and a CCN spectrum (section 6).

Spectral dispersions derived from in-cloud measurements, from our modeling of differential activation followed by internal mixing, and from the retrievals, are summarized in Table 5. The first row gives averages and standard deviations for the 36 analysis intervals. Values derived from modeling are in the third and fourth columns. To the left of these is the average derived using the CDP and that derived using CDP spectra corrected

for instrument broadening (section 4a). Even with the correction (second column), the dispersion based on the observations exceeds the model (third and fourth columns).

The fifth column gives the result based on Eq. (7), with σ_{obs} substituted for σ_{mod} and $\langle N_{obs} \rangle$ substituted for $\langle N_{mod} \rangle$. Here there is a large difference, relative to the value shown in the second column, but we do not view this as an inconsistency. Rather, the smaller dispersion derived using σ_{obs} and $\langle N_{obs} \rangle$ is qualitatively consistent with internal mixing having decreased the concentration variability resulting from differential activation. The dispersion presented in the sixth column was derived using Eq. (7) with σ_{ret} substituted for σ_{mod} and with $\langle N_{ret} \rangle$ substituted for $\langle N_{mod} \rangle$. This relatively large dispersion seems consistent with the view that the lidar-sensed parcels prior to mixing that occurred within the body of the cloud. However, we have also shown that a component of this variability can be attributed to departure from the $\langle \sigma_g \rangle = 1.4$ assumption (section 5d).

Results presented in Table 5 suggest that two model-derived statistics (σ_{mod} and $\langle N_{mod} \rangle$), and Eq. (7) can be used to generate dispersions that are approximately consistent with corrected spectral measurements. When the dispersions from each analysis interval are used to compute ratios of the modeled dispersion divided by the corrected measurement and these ratios are averaged the result is $\overline{x} = 0.74$ (± 0.29, segment count = 36). We interpret this average as indicating that differential activation and internal mixing can explain much of the dispersion within clouds during VOCALS. However, this conclusion is tentative because the correlation of modeled and corrected dispersions lacks statistical significance (i.e., $p > 0.05$). This lack of correlation may result from the separation between the below-cloud and in-cloud segments, but given that observed and modeled concentrations correlate (Fig. 12, $p < 0.05$), other factors may have contributed to the decorrelation. In particular, we suspect that measurement error may have played a role. Our reason for this suspicion is that independently measured dispersions varied by $\pm 30\%$,
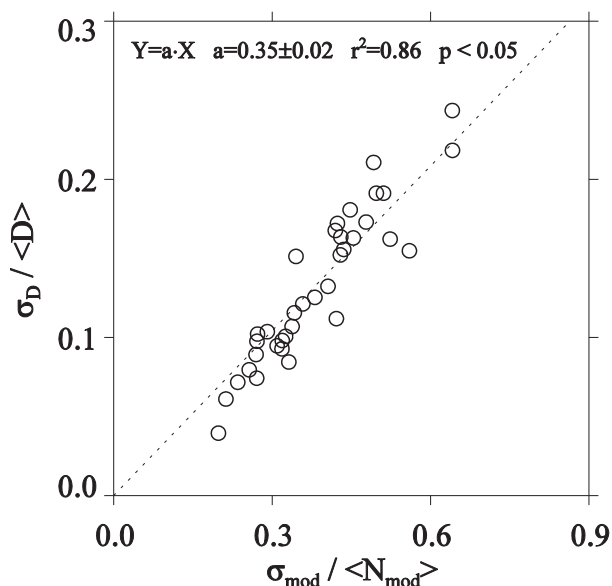

FIG. 13. Modeled spectral dispersions vs modeled concentration dispersions. The ordinate and abscissa values were derived from parcel model simulations (unweighted model) with the internal mixing hypothesis. The y deviations are the basis for the least squares criterion of best fit (Young 1962). The confidence interval on the fitted coefficient was derived using Student's t distribution at the 95% level (Havlicek and Crain 1988).The significance of the Pearson correlation coefficient r was evaluated in a two-tailed test using Student's t distribution at the 95% level (Havlicek and Crain 1988).

while the concentration variance is smaller ($\pm 10\%$; section 4a).

In their correlation of modeled and observed spectral standard deviations σ_D, with the former derived using a model of differential activation followed by internal mixing, Hudson et al. (2012) obtained a significant correlation ($p < 0.03$) for samples with LWC values between 0.84 and 1.61 of adiabatic (their Fig. 7b). In addition, Fig. 7b in Hudson et al. (2012) reveals a ratio of the modeled σ_D to the observed σ_D that is about a factor of 2 smaller than the ratio $\overline{x} = 0.74$ reported above. Part

TABLE 5. Spectral dispersions. Instrument broadening was corrected by applying the technique developed by Politovich (1993). This is described in section 4a.

	Basis: Observed in-cloud spectra	Basis: In-cloud observed σ_D corrected for instrument broadening	Basis: Parcel model spectra composited into a mixture spectrum	Basis: Values of σ_{mod} and $\langle N_{mod} \rangle$ and Eq. (7)	Basis: Values of σ_{obs} and $\langle N_{obs} \rangle$ and Eq. (7)	Basis: Values of σ_{ret} and $\langle N_{ret} \rangle$ and Eq. (7)
Avg and std dev for all 36 analysis intervals	0.25 ± 0.09	0.19 ± 0.07	0.13 ± 0.05	0.13 ± 0.04	0.07 ± 0.02	0.23 ± 0.09
Avg and std dev for the 8 analysis intervals with $SS_{eff} > 0.1\%$	0.19 ± 0.06	0.16 ± 0.06	0.09 ± 0.02	0.10 ± 0.02	0.07 ± 0.01	0.33 ± 0.14

of this discrepancy is because we formulated our ratio using broadening-corrected dispersions, while Hudson et al. (2012) formulated theirs using spectral standard deviations that were not corrected. Another difference is that Hudson et al. (2012) made their measurements in maritime cumulus where updrafts are generally larger than in maritime stratocumulus. That is, larger updraft increases SS_{eff}, and if this increase takes the SS_{eff} past the change in the slope of the activation spectrum, at approximately $SS = 0.1\%$ (Fig. 5a), it is expected that the relative variation of modeled concentrations will diminish and the mixture's dispersion will decrease (Warner 1969; Cooper 1989; Hudson and Nobel 2014). This inference was verified in our dataset by selecting dispersions associated with $SS_{eff} > 0.1\%$ (Table 2); results are shown in the second row of Table 5, where it is apparent that the modeled dispersion (third column) decreased slightly more than the broadening-corrected dispersion. With the condition $SS_{eff} > 0.1\%$, a larger decrease is also evident in the modeled σ_D relative to the broadening-corrected σ_D; however, because of our emphasis on spectral dispersion, we chose to not show that result.

Ultimately we need to test our description of spectral broadening. This is challenging because we averaged over in-cloud segments with extent much larger than the mixing process length scale. We demonstrated that airborne lidar can be used to probe stratocumulus at a scale that is likely relevant to the mixing ($\sim 40\,\text{m}$ horizontally), but our retrieval methodology applied a constant spectral width (i.e., $\langle \sigma_g \rangle = 1.4$); continued research is needed to achieve the goal of retrieving both N and σ_g using airborne lidar. We also demonstrated that $(1/3)(\sigma_{obs}/\langle N_{obs} \rangle)$ is smaller than the dispersion from a corrected measurement ($[\sigma_D]_{corrected}/\langle D \rangle$; Table 5) and concluded that this difference is consistent with the action of differential activation and internal mixing. Here we show how this conclusion changes when we analyze the in-cloud data at a scale smaller than the length of the in-cloud segments. Figure 14 shows CDP measurements from the example in-cloud segment. First, we note that values of N coincident with $LWC < 0.02\,\text{g m}^{-3}$ (at $\sim 1015{:}30$ and $\sim 1020{:}30$ UTC) are removed from Fig. 14b (section 4a) and from the averaged values displayed in Figs. 14c and 14d. Figure 14c has a gray band representing $\langle N_{obs} \rangle \pm 1\sigma_{obs}$ and black rectangles representing the average ± 1 std dev for subsets defined by 11 adjacent CDP samples. Figure 14d shows the value of $(1/3)(\sigma_{obs}/\langle N_{obs} \rangle)$ (gray line) (based on values of $\langle N_{obs} \rangle$ and σ_{obs} derived for the complete in-cloud segment) and values of $(1/3)(\sigma_{obs}/\langle N_{obs} \rangle)$ for the subsets (short black lines). The average of the ratios of the latter, divided by the former, is 0.78. When calculated for all

36 analysis intervals, and, averaged, this ratio is 0.70 ± 0.14. Also, the average of $[\sigma_D]_{corrected}/\langle D \rangle$ does not change when grouped into subset intervals and averaged (not shown). Hence, we conclude that the inequality $(1/3)(\sigma_{obs}/\langle N_{obs} \rangle) < [\sigma_D]_{corrected}/\langle D \rangle$ strengthens when the in-cloud CDP concentration measurements are averaged at a scale ($\sim 1.2\,\text{km}$) that is smaller than that of the in-cloud segments ($\sim 60\,\text{km}$).

8. Conclusions

We have presented an analysis of interrelations among CCN, updraft, and cloud microphysical properties within cloud-topped boundary layers over the southeastern Pacific Ocean. Most of the 36 analysis intervals consisted of below-cloud and in-cloud flight segments separated by approximately 100 km. Droplet concentrations retrieved using lidar and use of cloud geometric thickness from lidar and radar are the novel aspects of our analysis.

In-cloud concentrations (observations) and modeled concentrations correlate, but the latter are positively biased. These modeled concentrations are averages of parcel model output [Eq. (5a)]. A correction factor derived using airborne remote sensing and in situ thermodynamics is used to scale the modeled concentrations, and the application of the correction factor is shown to bring modeling and observation into agreement.

Modeled concentrations are also calculated as an updraft-weighted average of parcel model output [Eq. (5b)]. These updraft-weighted model concentrations are tabulated, and we show how they can be used to evaluate the flux of droplets entering a cloud-model grid box.

Concentrations are also retrieved using an airborne lidar. We show that error propagating into the retrieved concentration varies from -50% to $+29\%$ depending on the value of the geometric standard deviation of droplet size applied in the retrieval.

In our investigations of spectral broadening we demonstrate that two model-based formulations of the dispersion in droplet sizes are consistent. One of these is simpler to compute and this result may be useful for describing the effects of differential activation (Stevens et al. 1996) and internal mixing (Hudson and Svensson 1995) within multidimensional cloud models.

Because internal mixing of parcels is assumed, the relevance of our findings to actual clouds is contingent on the degree to which this does occur. Evidence for this is seen in our finding that a dispersion based on a concentration average $\langle N_{obs} \rangle$, a concentration variability σ_{obs}, and Eq. (7) is substantially smaller than either the
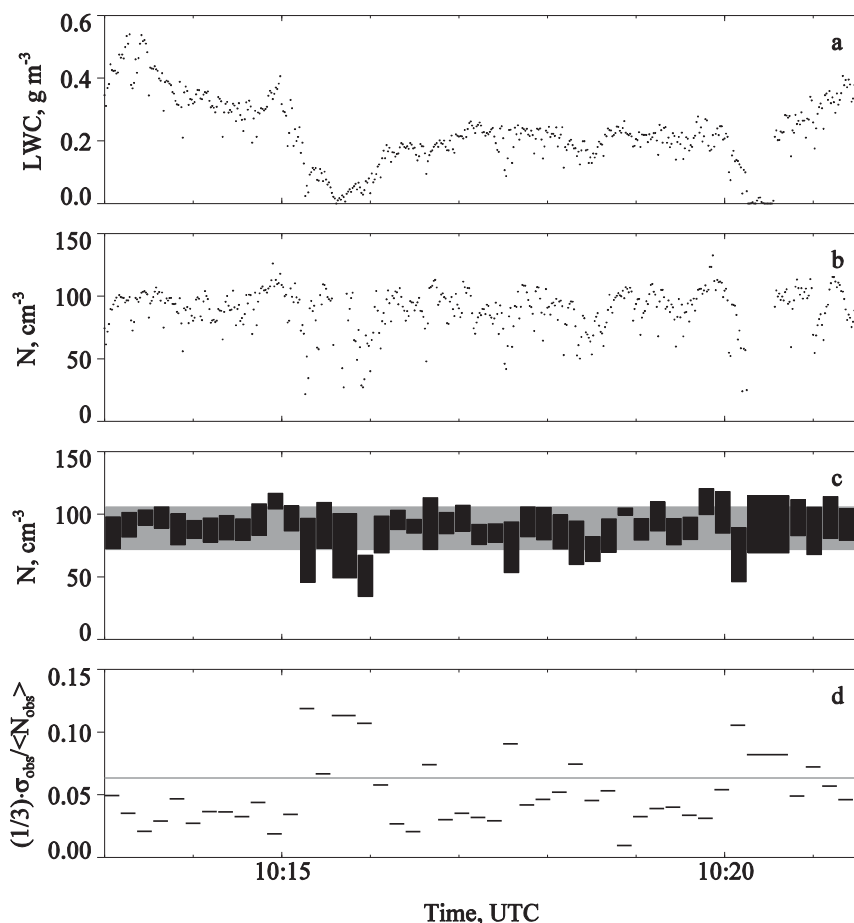
FIG. 14. The 1-Hz CDP measurements from the example in-cloud segment. (a) Liquid water content. (b) Cloud droplet concentration. (c) Gray band represents $\langle N_{\mathrm{obs}} \rangle \pm 1\sigma_{\mathrm{obs}}$; black rectangles represent the average $\pm$ 1 std dev for 11-sample subsets. (d) Gray line is $(1/3)(\sigma_{\mathrm{obs}}/\langle N_{\mathrm{obs}} \rangle)$ calculated using the values $\langle N_{\mathrm{obs}} \rangle$ and σ_{obs} for the complete in-cloud segment; short black lines are the same, but for subsets.

size dispersion from corrected droplet spectra or the size dispersion from modeled spectra (Table 5). This has relevance to prior investigations where concentration variability, derived using in-cloud observations, was smaller than that derived with a model of differential activation (Snider and Brenguier 2000; Romakkaniemi et al. 2009). The present findings suggest that $(1/3)(\sigma_{\mathrm{obs}}/\langle N_{\mathrm{obs}} \rangle)$ may range between an upper limit [rhs of Eq. (7)], when parcels activating at different updrafts are not mixed, and zero in the limit of complete internal mixing.

In addition, we showed that the model-derived size dispersion is, on average, 74% of the size dispersion from corrected droplet spectra. Although this does not implicate differential activation and internal mixing as dominant for spectral broadening, it does suggest that they play an important role. Other relevant processes involve the mixing of adiabatic and nonadiabatic

trajectories (Cooper 1989; Politovich 1993; Cooper et al. 2013), internal mixing of parcels that reach the LCL at different altitudes (J. Wang et al. 2009), adiabatic recirculation of cloudy parcels (Korolev 1995), and CCN spectral amplitude and shape (Hudson and Yum 1997). Since the dispersion is an important factor in predictions of drizzle formation (Beheng 1994; Austin et al. 1995; Liu and Daum 2004) and in predictions of cloud albedo (Liu and Daum 2002), and because there is an ongoing debate about how to parameterize the dispersion in cloud models (Hudson and Yum 1997; Liu and Daum 2002; Pawlowska et al. 2006; Lu et al. 2007), we expect that our findings will advance understanding of stratocumulus microphysics.

TABLE A1. Threshold–diameter tables used for the PCASP and F300. Thresholds are an internal electronic representation of the channel boundaries (Cai et al. 2013).

PCASP, $n = 1.59$			F300, $n = 1.59$			F300, $n = 1.33$		
Threshold	Lower D (μm)	Upper D (μm)	Threshold	Lower D (μm)	Upper D (μm)	Channel	Lower D (μm)	Upper D (μm)
692	0.109	0.117	38	0.25	0.28	0	0.31	0.35
1040	0.117	0.125	92	0.28	0.32	1	0.35	0.40
1517	0.125	0.133	194	0.32	0.37	2	0.40	0.46
2157	0.133	0.141	376	0.37	0.42	3	0.46	0.51
4096	0.141	0.157	678	0.42	0.48	4	0.51	0.57
4231	0.16	0.17	1155	0.48	0.53	5	0.57	0.64
4348	0.17	0.19	1880	0.53	0.58	6	0.64	0.68
4537	0.19	0.21	2942	0.58	0.64	7	0.68	0.73
4825	0.21	0.23	4096	0.64	0.70	8	0.73	0.80
5251	0.23	0.25	4140	0.70	1.06	9	0.80	1.02
5859	0.25	0.27	4238	1.06	1.80	10	1.02	2.46
6703	0.27	0.29	4384	1.80	2.43	11–13	2.46	4.69
8192	0.29	0.31	4590	2.43	3.45	14–16	4.69	6.85
8345	0.31	0.45	4699	3.45	4.11	17–19	6.85	9.28
8502	0.45	0.62	4807	4.11	4.79	20, 21	9.28	11.3
8682	0.62	0.71	4928	4.79	5.58	22–24	11.3	12.9
8872	0.71	0.79	5027	5.58	6.67	25–28	12.9	15.2
9070	0.79	0.88	5124	6.67	7.73	29	15.2	17.7
9252	0.88	0.97	5255	7.73	8.72			
9432	0.97	1.06	5446	8.72	9.66			
9544	1.06	1.20	5673	9.66	10.7			
9737	1.20	1.37	5912	10.7	11.6			
9937	1.37	1.53	6164	11.6	12.6			
10 166	1.53	1.69	6429	12.6	13.6			
10 471	1.69	1.85	6754	13.6	14.6			
10 797	1.85	2.00	7027	14.6	15.6			
11 162	2.00	2.23	7310	15.6	16.7			
11 499	2.23	2.46	7601	16.7	17.8			
11 852	2.46	2.71	7901	17.8	18.9			
12 288	2.71	3.04	8192	18.9	20.0			

APPENDIX A

Aerosol Particle Hygroscopicity

Information about aerosol hygroscopicity, used in the parcel model, comes from dried-particle and haze-particle spectra recorded during the below-cloud segments. In what follows, we analyze airborne measurements of the dried and humidified spectra using the dual-OPC technique developed by Snider and Petters (2008). At the end of this section we derive the hygroscopicity value we used to model the Köhler curves of particles with dry diameter greater than 0.11 μm.

For VOCALS, we have improved the dual-OPC technique in two ways. First, we evaluated the OPCs' (PCASP and F300) response to mobility-classified particles, and, in the case of the PCASP, we adjusted the manufacturer-recommended sizing. Second, we accounted for a difference between the OPCs' threshold–diameter relationship derived during laboratory calibration and that applied during data acquisition onboard the C-130. These improvements are documented in appendix B, where we also note that the data archive maintained by NCAR does not account for either correction. The calibrated threshold–diameter relationships (PCASP and F300), assuming refractive index $n = 1.59$ particles and operation onboard the C-130, are provided in Table A1. A sizing relationship is also provided for the F300's
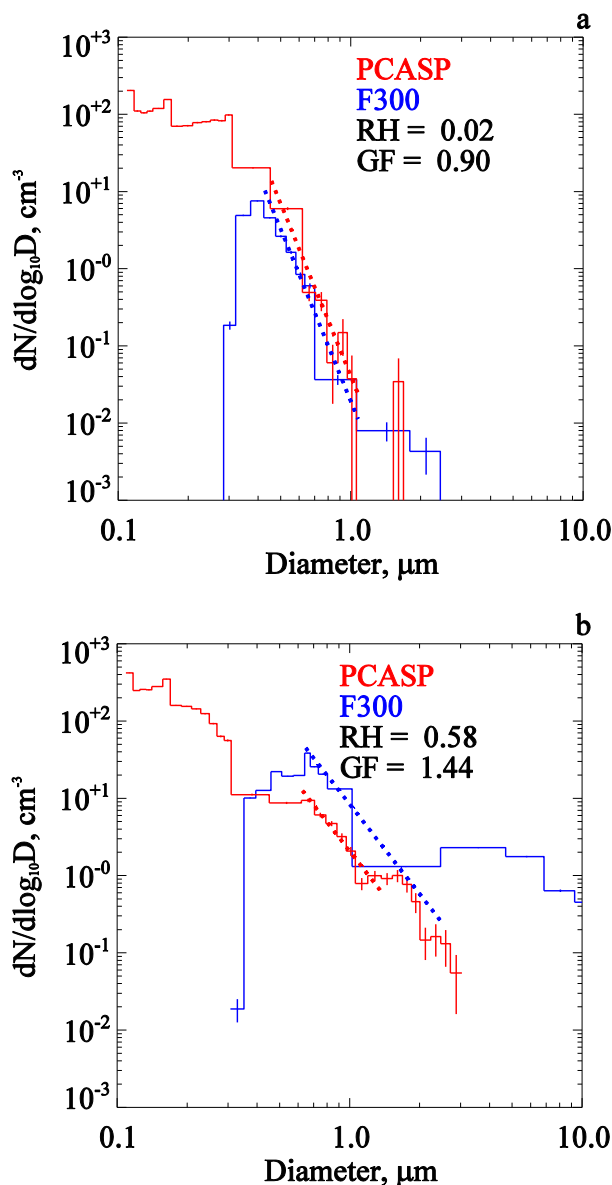
FIG. A1. (a) Above-cloud aerosol size spectra, PCASP and F300, for the example above-cloud segment (RF05; 1000–1010 UTC). Particle refractive index n is assumed equal to 1.59 in both OPCs. (b) Below-cloud spectra, PCASP and F300, for the example below-cloud segment (RF05; 1028–1041 UTC). Particle refractive index is assumed at $n = 1.59$ and 1.33 in the PCASP and F300, respectively.

assessment of the haze particles; for this, we applied $n = 1.33$ (Snider and Petters 2008). For wet diameters greater than $2.5\,\mu$m, adjacent F300 channels were combined to account for ambiguity due to the nonmonotonic relationship between particle size and forward scattering intensity.

Fig. A1a presents the PCASP and F300 aerosol size spectra from the example above-cloud segment. Here we applied the threshold–diameter relationships for $n = 1.59$ particles. The blue and red vertical error bars, most

visible on the spectra at $D > 1\,\mu$m, denote the Poisson sampling uncertainty. Given this uncertainty, it is evident that an interprobe comparison is not possible for diameters larger than about $1\,\mu$m. Also, for particles smaller than $0.4\,\mu$m, comparison is not possible because of the nonphysical roll off of the F300 spectrum compared to the PCASP spectrum. Also shown are power-law fits of the spectra (dotted red and blue lines). Following Snider and Petters (2008), these fit lines were used to derive a hygroscopic growth factor (GF). Provided we have set the sample area of the F300 correctly at $A_F = 0.10\,\text{mm}^2$ (appendix B), we expect this GF to be close to unity in the dry above-cloud air. This is indeed the case for the example presented in Fig. A1a (RH = 2%). For all of the above-cloud segments the average GF is 1.01 ± 0.10.

Fig. A1b presents PCASP and F300 spectra from the example below-cloud segment. As in our analysis of the above-cloud segments, we assume that the PCASP particles are dried and that $n = 1.59$ (Strapp et al. 1992). Also, consistent with the prior discussion, the haze particles measured by the F300 are assigned $n = 1.33$, and adjacent channels at $D > 2.5\,\mu$m are combined to account for ambiguity due to the nonmonotonic relationship between particle size and forward scattering intensity. The derived GF, written on Fig. A1b, demonstrates that the ambient particles are approximately 40% larger by virtue of their hygroscopic growth at RH = 58%.

Our 36 determinations of the below-cloud GF are summarized in Fig. A2a. As in Snider and Petters (2008), these assessments are bounded by predictions, which in the upper-limit indicate that the dried particles are equivalent to particles composed of sodium sulfate and in the lower limit indicate an equivalence to a mixture (by mass) of 60% sodium sulfate and 40% nonhygroscopic component. Consistency with our prior estimates of the hygroscopicity of marine particles (Snider and Petters 2008) is encouraging but does not preclude the possibility of bias. Possible sources of bias are the OPC calibrations (appendix B), the OPC measurements, and our refractive index assumption. For one of the data values we illustrate the GF uncertainty estimated by Snider and Petters (2008). Given the overall consistency of our result with Snider and Petters (2008), our uncertainty estimate may be too conservative.

In Fig. A2b we present the measurements again, but here with a GF prediction based on a different parameterization of sodium sulfate's hygroscopicity (Kreidenweis et al. 2008; $\kappa = 0.74$). A comparison of the solid curves (Figs. A2a,b) reveals a GF disagreement for the same aerosol composition (pure Na_2SO_4). This disagreement can be traced to differences between the
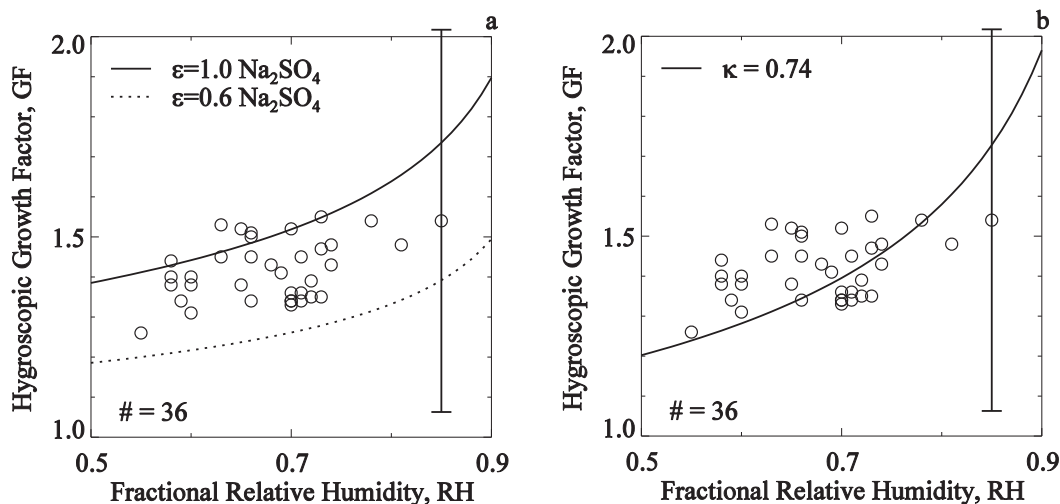
FIG. A2. (a) GF measurements vs ambient RH and predictions based on Snider et al. (2003) with two hygroscopic mass fractions ($\varepsilon = 1$ and $\varepsilon = 0.6$), the Na_2SO_4 parameterization from Tang and Munkelwitz (1994), and density of the nonhygroscopic fraction equal to $1200\,kg\,m^{-3}$. (b) Data points repeated from (a). Here the line is a model prediction based on Petters and Kreidenweis [2007; their Eq. (11)] with $\kappa = 0.74$ for Na_2SO_4 (Kreidenweis et al. 2008). The GF uncertainty from Snider and Petters (2008) is also indicated for one of the data points.

water activity parameterizations used to construct the two curves. We note that the difference is quite large at an RH representative of the below-cloud segments but decreases with increasing RH to a minimal difference at RH = 90%. Consistent with results shown in Fig. A2b, the value $\kappa = 0.74$ was accepted as the project average and was used in the parcel model to describe the Köhler curves of particles with dry diameter greater than $0.11\,\mu m$. These are the particles sized and counted by the PCASP (Table A1).

APPENDIX B

Optical Particle Counter Calibration

This appendix summarizes our calibrations of two optical particle counters (OPCs). This work was conducted in 2008 and 2011 in our laboratory at the University of Wyoming (UWYO). The instruments are a model 300 Forward Scattering Spectrometer Probe [F300; serial number (SN) = 25665–0991–05] and a Passive Cavity Axially Scattering Probe (PCASP; SN = 23738–0491–08). Both have the Signal Processing Package (SPP), developed by Droplet Measurement Technologies (DMT; Boulder, Colorado), both are owned by NCAR, and both are installed in an external pod during airborne operations. During two intervals, in 2008 and 2011, these OPCs were installed on the NCAR C-130 aircraft for the VOCALS (October and November 2008) and the Ice in Clouds Experiment–Tropical

(ICE-T; June and July 2011) campaigns. The F300 and PCASP were fabricated by Particle Measuring Systems (PMS; Boulder, Colorado), a predecessor of DMT; the latter company services both instruments.

We describe test particle generation (section Ba), data recording (section Bb), the sample area, and the channel–diameter relationships we used to analyze C-130 measurements made with the F300 [sections Bc(1)–Bc(3)], and the aerosol flow and the channel–diameter relationships we used to analyze C-130 measurements made with the PCASP [sections Bd(2) and Bd(3)]. The PCASP inlet system is described in section Bd(1).

a. Methods

Measurements were made in the Department of Atmospheric Science at the University of Wyoming. The aerosol generation system and the aerosol detection instrumentation are shown in Fig. B1. OPC testing was conducted using particles that were size selected based on their electrical mobility. Test aerosol preparation started with pneumatic atomization of a hydrosol containing polystyrene latex (PSL) spheres. The resulting dispersion was dried, charge neutralized, size classified in a TSI DMA3081 electrostatic classifier (TSI 2000), and diluted. In addition to spectra measurements from the OPCs, spectra were measured with a Scanning Mobility Particle Sizer (SMPS) and size-integrated concentrations were measured with a condensation particle counter (CPC). Cai et al. (2013) provide descriptions of the SMPS and CPC used in this testing.
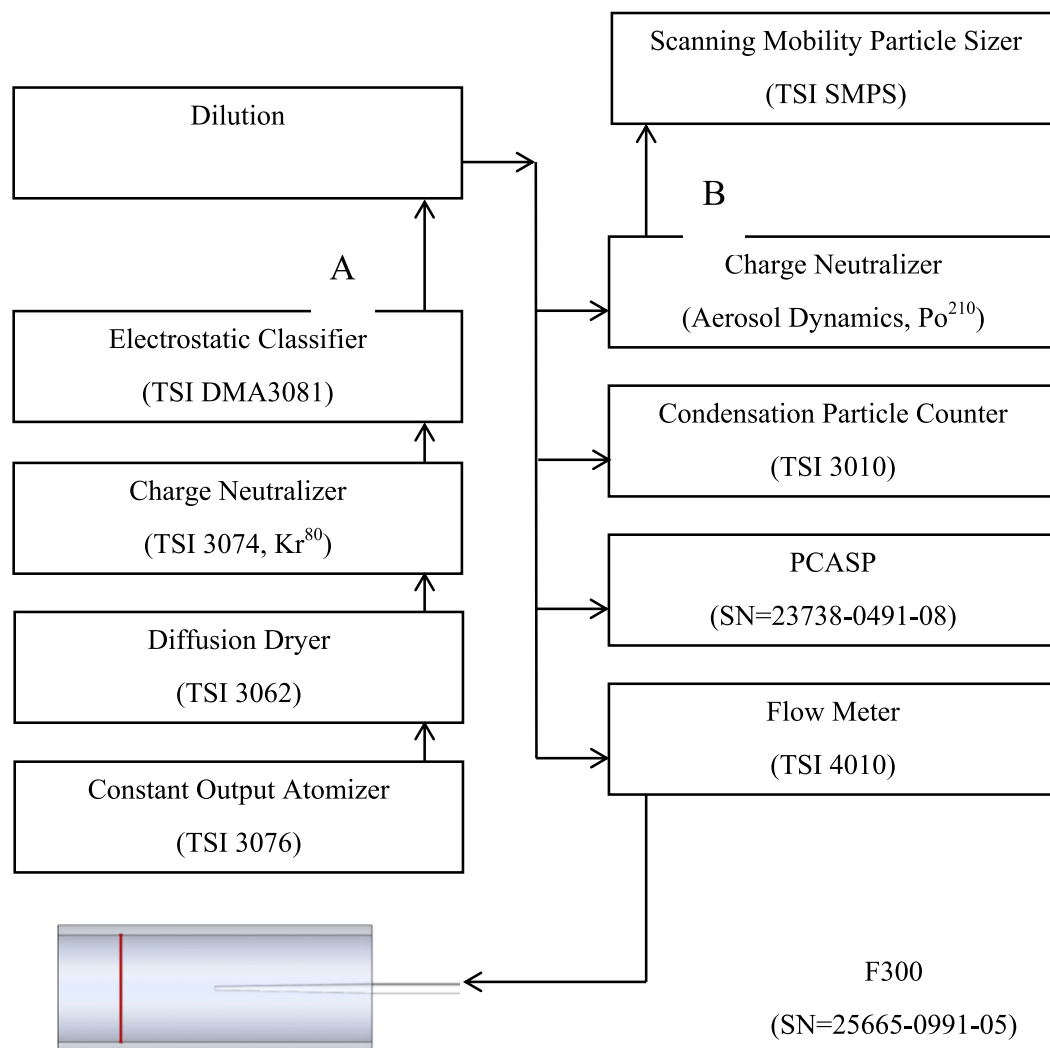
FIG. B1. Schematic diagram of the particle generation and measurement systems.

b. Data acquisition

The particle count histograms produced by the F300 were recorded using the Particle Analysis and Collection Software (PACS; DMT, Inc.); a histogram was recorded every second (1-Hz sampling). Spectra were also obtained using the SMPS (Fig. B1). These were recorded using the Aerosol Instrument Manager software (TSI, Inc.) as a 300-s average (Cai et al. 2013). In addition, a Labview Virtual Instrument (National Instruments, Inc.) recorded the size-integrated concentrations (CPC), aerosol flowrates (TSI 4010; Fig. B1), the PCASP aerosol flowrates, and the PCASP count histograms. The Labview-recorded signals were sampled at 1 Hz.

c. F300

Fig. B1 shows a convergent tube (from 3- down to 1-mm inner diameter) that was used to accelerate particles across the F300's laser. The position of the tube was adjusted so that the particle count rate, reported by the F300, was a maximum. The particle speed exiting this tube was assumed to be the airspeed at the tube's exit (Fig. B1). Because a range of dilution airflow rates were used in the laboratory tests (Fig. B1), there were a range of particle speeds; values were between 2 and 25 m s^{-1}. Unfortunately, the tube's exit cross section (0.8 mm^2) is larger than the F300's sample area [section Bc(1)], so we were unable to direct particles exclusively into the sample area.

1) F300 SAMPLE AREA

An outstanding problem with the F300 is the difficulty of determining the portion of its laser beam that produces an unambiguous scattering signal. We note that the F300's laser beam is oriented perpendicular to the C-130's line of flight and that three dimensions are defined

TABLE B1. Summary of laboratory measurements of particle size. Thresholds are an internal electronic representation of the channel boundaries (Cai et al. 2013). The average relative difference is formulated in terms of the PSL diameter $D_{i,\text{PSL}}$ and the midpoint diameter of the channel with the maximum histogram value. The latter is given as $D_{i,X}$, where i is the test number and X is a place holder for SMPS, F300, or PCASP. In terms of these symbols, the average relative difference is $\langle Y \rangle = n^{-1}\sum Y_i$, where Y_i is $|D_{i,\text{PSL}} - D_{i,X}|/D_{i,\text{PSL}}$ and n represents the number of tests.

Test particle diameter	Particle sizing instrument	Threshold–diameter table	Average relative difference	No. of tests
342-, 491-, and 707-nm PSL	SMPS	—	0.01	59
342-, 491-, and 707-nm PSL	F300	Manufacturer	0.09	59
125-, 152-, 199-, 491-, and 707-nm PSL	PCASP	Adjusted	0.03	47

relative to the beam. One of these is along the beam axis (the longitudinal dimension), and the other two are perpendicular (the transverse dimensions). Distances along the three dimensions characterize the F300 sample volume. Also, we note that the probe's sample volume is defined operationally: particles that produce an in-focus scattering signal pass through the sample volume, and those that produce an out-of-focus scattering signal (or negligible scattering signal) do not pass through the sample volume. The two relevant possibilities (in focus and out of focus) are distinguished by the probe's microprocessor. The basis for the distinction is the microprocessor's analysis of time-dependent scattering signals reported by a partially masked and unmasked photodetector (Baumgardner et al. 1992).

During airborne operation, one of the sample volume's transverse dimensions is set by the C-130's true airspeed and the data averaging time interval. The latter, in most applications, is 1 s (1-Hz sampling). The sample volume's two other dimensions are the optical depth of field, measured longitudinally and the second transverse dimension, commonly known as the laser beam height. The product of the depth of field and the beam height define the probe's sample area A_F. Baumgardner et al. (1992) evaluated A_F by correlating the F300 particle count with particle concentration values reported by a model 100 Forward Scattering Spectrometer Probe. More recently, we determined the A_F by correlating measurements of F300 count and PCASP concentration (Snider and Petters 2008).

We applied the technique of Snider and Petters (2008) and determined project-averaged A_F values. These are 0.10 and 0.07 mm^2 for VOCALS and ICE-T, respectively. We note that these determinations of A_F are about a factor of 2 larger than previously published estimates (Baumgardner et al. 1992; Snider and Petters 2008). This shift resulted because the previous estimates were based on the manufacturer's calibration of the threshold–diameter relationship for the PCASP and on the manufacturer's calibration of the PCASP's aerosol flow system. Both here [sections Bd(2) and Bd(3)] and in Cai et al. (2013), we document significant differences between our calibrations of these probe characteristics

and the manufacturer's. The values of A_F archived in the Network Common Data Format (NetCDF) files, released by NCAR, are about 50% larger than the values $A_F = 0.10$ mm^2 (VOCALS) and $A_F = 0.07$ mm^2 (ICE-T) we are recommending here.

2) F300 LABORATORY TEST DATA

The F300-derived test particle spectra are presented online (http://www.atmos.uwyo.edu/~jsnider/LINK-F300.pdf). This set of figures is a composite of 59 tests. Results are arranged chronologically from May 2009 to August 2011; tests with PSL diameters equal to 343, 491, and 707 nm are reported. Included for each test are spectra (300-s average) from the SMPS and F300 (left panel) and the count histogram from the F300 (right panel, also a 300-s average). The vertical dashed line (left panel) is the diameter of the test particles. This diameter is set by the PSL manufacturer's specification (Duke Scientific Corporation) and by the fact that we select the test particle diameter, at the nominal PSL size, using an electrostatic classifier (Fig. B1).

As summarized in Table B1, good agreement was obtained in a comparison of the PSL diameter D_{PSL} and the mode diameter reported by the SMPS D_{SMPS}. The average relative difference for that comparison is 0.01 or 1%. Also, in Table B1, we present a statistical summary of the comparisons of D_{PSL} versus D_{F300} and D_{PSL} versus D_{PCASP}. Those results are discussed in sections Bc(3) and Bd(3), respectively.

From our analysis of the F300 spectra (http://www.atmos.uwyo.edu/~jsnider/LINK-F300.pdf), we reached two additional conclusions. The first is related to particle charge state within the aerosol generation system. At point A (Fig. B1) most of the test particles are singly charged, and most have a diameter equal to the prescribed PSL diameter. When transiting toward the SMPS, the particles pass through a neutralizer, where a Boltzmann charge state is reestablished (TSI 2000). Subsequent to the neutralizer, and prior to entering the cylinder of the SMPS, at point B, both +1 particles and multiply charged particles (+2, etc.) are present. With knowledge of the PSL particle diameter, we calculated the mobility-equivalent diameter of the multiply
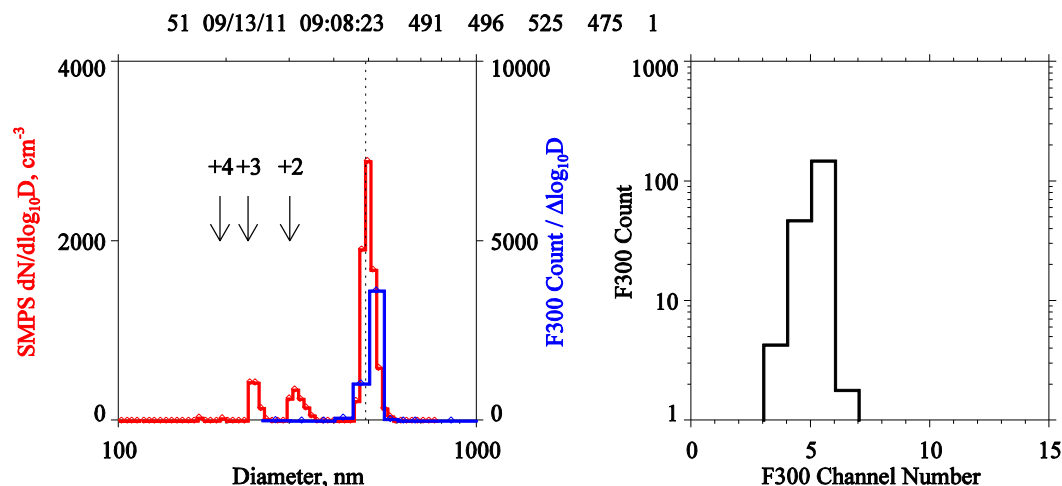
51   09/13/11   09:08:23   491   496   525   475   1

FIG. B2. Laboratory spectra selected from the set of 59. The test particles are mobility-selected PSL particles at D_{PSL} = 491 nm [(left) vertical dashed line]. Downward arrows indicate the mobility-equivalent size of multiply charged 491-nm PSL particles. The ''Reject-Based-on-Depth-of-Field'' option is set to ''yes.'' See text for details.

charged particles (Snider et al. 2010). Those diameters are indicated with downward arrows in the left panels of the figures at http://www.atmos.uwyo.edu/~jsnider/LINK-F300.pdf.

In Fig. B2 we present a specific example of the situation described in the previous paragraph. Here the test particles are 491-nm PSL. We see that the F300 and SMPS both respond at close to the nominal PSL diameter. We also see that particles at 300 nm are detected by the SMPS, but not by the F300. This example makes it clear that the particles detected by the SMPS, at the diameters indicated by the downward arrows, actually have a diameter equal to D_{PSL}, but because they are multiply charged, they are sized at a smaller mobility-equivalent diameter. Such ambiguity is a

consequence of the SMPS's discrimination of particles based on their electrical mobility and the fact that electrical mobility depends on both a particle's size and its charge state.

Our second finding relates to a user-selectable option for F300 measurements acquired by the PACS (section Bb). When setting up the PACS the user can select either ''yes'' or ''no'' for the option Reject-Based-on-Depth-of-Field. In our dataset we have 37 tests with the ''Reject-Based-on-Depth-of-Field'' option set to ''yes'' (in-focus detections only) and 22 with the option set to ''no'' (both in-focus and out-of-focus detections). If ''yes'' is selected, then only the in-focus detections are registered into the histogram produced by the PACS. If ''no'' is selected, then all detections (in focus and out of
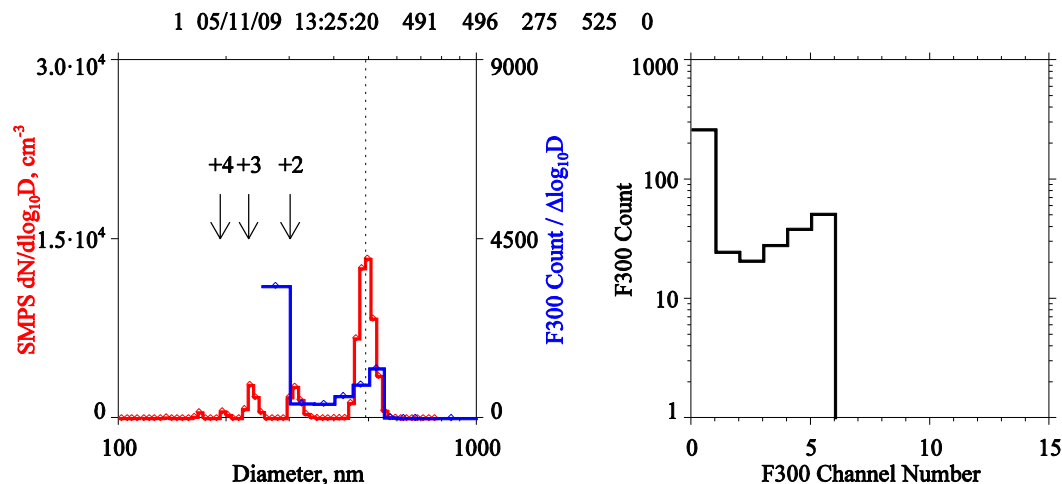
1   05/11/09   13:25:20   491   496   275   525   0

FIG. B3. As in Fig. B2, but with the ''Reject-Based-on-Depth-of-Field option'' set to ''no.'' The test particles are mobility-selected PSL particles at D_{PSL} = 491 nm [(left) vertical dashed line].
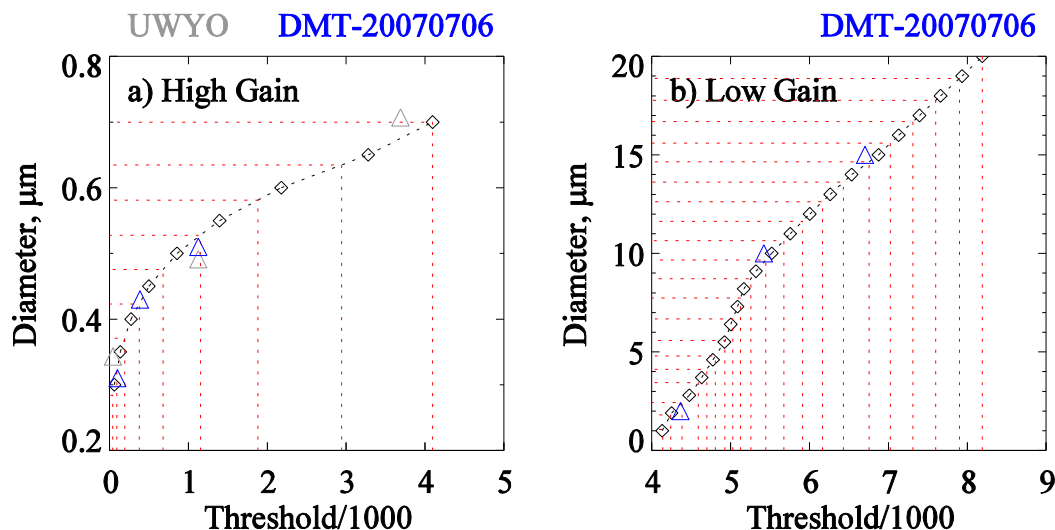
FIG. B4. Summary of F300-based particle sizing tests performed at DMT and UWYO. The dotted black line connecting diamonds is the manufacturer's threshold–diameter table, the vertical red dashed lines are the C-130 thresholds, and the blue and gray triangles are the channels that PSL spheres classify into. The latter are plotted at the midpoint of the channel with the maximum histogram value.

focus) are registered. An example spectrum, acquired with the option set to "no," is shown in Fig. B3. It is evident that most of the F300 detections were classified in channel 0. By comparing Fig. B3 and Fig. B2, where "yes" is selected and the test particle size is the same (491 nm), we infer that the in-focus detections correspond to the minor F300 mode at channel 5 in Fig. B3. "Yes" for the option "Reject-Based-on-Depth-of-Field" was used onboard the C-130.

3) F300 SIZING TESTS

Spectra corresponding to the "no" tests, and the "yes" tests, and for all test particle sizes ($D_{PSL} = 343, 491$, and 707 nm), were analyzed. Consistent particle sizing results were obtained for testing conducted in 2008 and in 2011. The supplementary material has 14 tests with 343-nm particles, 30 tests with 491-nm particles, and 15 tests with 707-nm particles (http://www.atmos.uwyo.edu/~jsnider/LINK-F300.pdf). Without exception, a histogram mode can be observed in the zeroth channel (343-nm particles), in the fifth channel (491 nm particles), and in the eighth channel (707-nm particles).

Fig. B4 summarizes the F300 sizing tests we performed and those conducted by DMT. The instrument has two gain stages, and results are split between calibrations for small particles (high gain, Fig. B4a) and large particles (low gain, Fig. B4b). Calibration data points are shown as triangles, with gray and blue indicating calibrations conducted at UWYO and DMT, respectively. The triangles are plotted at the midpoint of the channel with the maximum histogram value.

Assignment of an array of thresholds to an array of diameters is contingent on properties of the OPC (laser illumination, scattering geometry, and photodetector signal amplification), and particle-dependent properties (index of refraction and shape). That assignment is provided by the instrument manufacturer and is referred to as the manufacturer's calibration. The latter is shown in Figs. B4a and B4b as a dashed black line connecting diamonds plotted at each of the 30 threshold–diameter pairs. Although there are some outliers, we document reasonable agreement between the manufacturer's calibration and the laboratory testing (i.e., the actual measurements made both at Laramie and at DMT). A statistical comparison of the PSL diameter D_{PSL} and the F300's channel midpoint diameter, based on the manufacturer's calibration, is shown in the second row of Table B1. It is apparent that the average relative difference is 0.09 or 9%. Compared to the result seen in the first row of Table B1 (0.01 or 1%), the average relative difference is larger. This reflects both the scatter of measurements about manufacturer's calibration (Figs. B4a,b) and the fact that the sizing resolution of the F300 is coarser than that of the SMPS (Cai et al. 2013). Given the reasonable consistency between laboratory testing and the manufacturer's calibration, we applied the manufacturer's threshold–diameter calibration to the C-130 measurements made in VOCALS and ICE-T. However, an adjustment is needed to fully incorporate our laboratory finding with the C-130 measurements.

The analysis discussed in the previous paragraph is based on measurements made with the F300
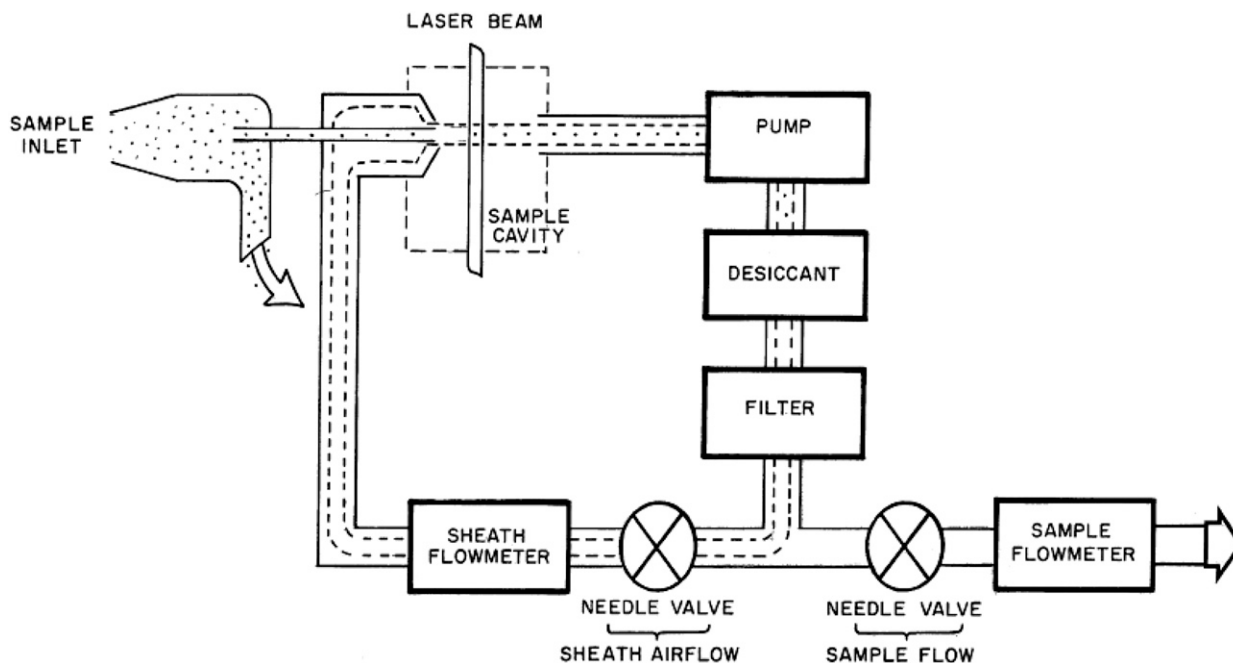
FIG. B5. The PCASP's sampling system (Particle Measuring Systems 2002).

operated with the manufacturer's threshold–diameter table. When the instrument is operated on the C-130 a nonconventional threshold–diameter table is used (D. Rogers 2009, personal communication). The C-130 threshold–diameter table is presented in Table A1. In Figs. B4a and B4b, the vertical red dashed lines illustrate the C-130 thresholds. It is apparent, particularly in Fig. B4a, that we evaluated the C-130 calibration diameters at the intersections of the C-130 thresholds (vertical red dashed line) and the manufacturer's threshold–diameter calibration.

A set of calibration diameters, somewhat different from that in Table A1, was archived in the NetCDF files released by NCAR. The diameters in the NetCDF archive of the VOCALS campaign are 4%–50% larger than our recommendation in Table A1. Users of the VOCALS and ICE-T datasets are encouraged to use the C-130 threshold–diameter table provided in Table A1. This table is the basis of our analysis of the VOCALS C-130 F300 measurements.

d. PCASP

1) PCASP HEATING OF THE AEROSOL SAMPLE

The PCASP's airflow system is designed to direct an aerosol stream across the probe's helium–neon laser (wavelength $\lambda = 0.633 \, \mu$m). Particle loss is minimized by directing the stream along a straight path from the sample inlet to the laser (Fig. B5). The aerosol stream first encounters the PCASP at the diffuser, where it is decelerated from the C-130's true airspeed ($\sim$110 m s^{-1}) to $\sim$11 m s^{-1} (Particle Measuring Systems 2002). The aerosol stream then passes through a narrow tube (inner diameter = 0.5 mm), where it is combined with sheath air; the combined flow then crosses the laser. The volumetric rate of the sheath stream is set to be 15 times the aerosol flowrate (Particle Measuring Systems 2002). Because of a nozzle restriction at the point where the flows are combined, the combined stream crosses the laser at approximately 45 m s^{-1} (Particle Measuring Systems 2002). The combined stream exits the sample cavity to a pump, is passed through a tube filled with granular desiccant, through a filter, and is then split. One of the streams is passed through the sheath flow valve, is monitored in a mass flowmeter, and is recirculated. The other stream is passed through the sample flow valve, is monitored in a mass flowmeter, and is dumped. Because of mass continuity, the mass flowrate monitored by the aerosol flowmeter is equivalent to the aerosol mass flowrate passing through the sample cavity. The devices used for the sheath and aerosol flow measurement are the model AWM3300V and AWM3100V mass flow meters (Honeywell).

In the previous paragraph, we mentioned the tube that carries the aerosol stream from the diffuser to the sample cavity. This tube is evident in Fig. B5 and will be referred to as the ''needle.'' The PCASP inlet is equipped with three deice heaters. These are automatically
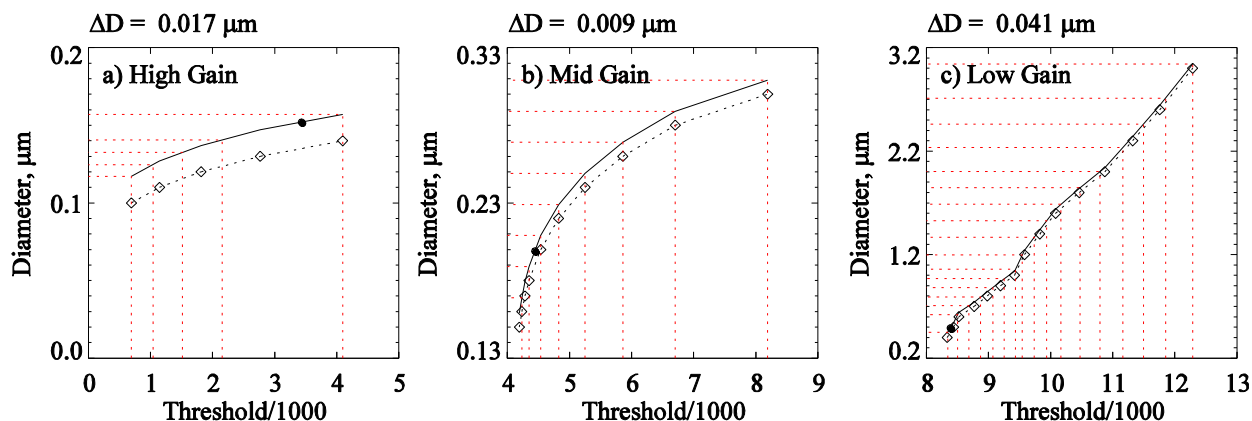
FIG. B6. Summary of PCASP-based particle sizing performed at UWYO. The dotted black line connecting diamonds is the manufacturer's threshold–diameter table, the vertical red dashed lines are the C-130 thresholds, and the filled circles are the channels into which the PSL spheres (0.152, 0.199, and 0.491 μm). The latter are plotted at the midpoint of the channel with the maximum histogram value. See text for details.

activated when the C-130 leaves the runway. The heaters are located near the tip of the diffuser (35 W), at the back of the diffuser (100 W), and in close proximity to the front end of the needle (10 W). Strapp et al. (1992) demonstrated that compressional warming, combined with heating due to the deice heaters, can have a substantial effect on the size of wet aerosol particles sampled by the PCASP. They estimated that particles reside sufficiently long within the decelerating stream, and within the probe, to lose most of their chemically bound water. Strapp et al. (1992) estimated the interaction time to be 0.2 s. Snider and Petters (2008) used a model similar to that employed by Strapp et al. (1992) and showed that particles starting at a wet diameter of 0.84 μm, corresponding to a haze particle equilibrated at RH = 96%, evaporate to 0.48 μm. In Strapp et al. (1992) and in Snider and Petters (2008), model RH $\leq$ 40% were assumed. Measurements are needed to validate this probe-RH assumption.

2) PCASP AEROSOL FLOWMETER CALIBRATION

The PCASP derives particle concentration as the ratio of the particle count rate (number of particles per second) and aerosol flowrate (actual cubic centimeters per second). The latter is derived in two steps. First, the signal from the PCASP's aerosol flow sensor, represented either as an analog signal [millivolt (mV); VOCALS], or as an integer (cnt; ICE-T), is used to derive the aerosol flowrate [standard cubic centimeter per second (sccps)]. The project-specific calibrations are

$$\text{sccps} = -0.0165 + (7.9354 \times 10^{-5}) \times \text{mV}$$
$$+ (1.1453 \times 10^{-7}) \times (\text{mV})^2 \quad (\text{VOCALS}) \quad (\text{B1})$$

and

$$\text{sccps} = 7.518\,85 + (-8.468\,21 \times 10^{-3}) \times \text{cnt}$$
$$+ (2.301\,30 \times 10^{-6}) \times (\text{cnt})^2 \quad (\text{ICE-T}). \quad (\text{B2})$$

In the second step, the standard flowrate value is converted to the ambient flowrate. This is done by evoking the ideal gas law with measurements of ambient pressure and temperature.

We evaluated the flowrate calibrations [Eqs. (B1) and (B2)] by correlating flow measurements (converted to standard pressure and temperature) with the signal output by the PCASP's aerosol flowmeter. The integer (cnt) and analog (mV) signals are relatable via a 12-bit analog-to-digital conversion.

3) PCASP SIZING CALIBRATION

PCASP's response to a known particle size was evaluated using PSL test particles (D_{PSL} = 125, 152, 199, 491, and 707 nm); results from 47 tests are shown online (http://www.atmos.uwyo.edu/~jsnider/LINK-PCASP.pdf). Evident in the left panels of this set of figures is a vertical dashed line, plotted at the diameter of the PSL test particle, with arrows indicating the mobility-equivalent diameter of the multiply charged test particles. The latter are described in section Bc(2).

Figure B6 summarizes the PCASP sizing calibrations. The probe has three gain stages, and therefore the results are split to show calibrations of the high-gain (Fig. B6a), midgain (Fig. B6b), and low-gain stages (Fig. B6c). Calibration data points are indicated as filled circles; these are plotted at the midpoint of the channel with the maximum histogram value. For all gain stages, and especially for the high-gain stage (Fig. B6a), we find that the manufacturer's calibration (dashed line connecting diamonds) underestimates particle diameter. Because of this, we have provided an adjusted threshold–diameter

calibration (solid line). A statistical comparison of laboratory determinations of particle size, based on the adjusted calibration, is shown in Table B1. It is apparent that the average relative difference is 0.03 or 3%.

The result summarized in the third row of Table B1 is based on measurements made with the PCASP operated with the adjusted threshold–diameter table. When the instrument is operated on the C-130 a nonconventional threshold table is used (A. Schanot 2009, personal communication). The C-130 thresholds are presented in Figs. B6a–c as vertical red dashed lines. It is apparent, particularly in Fig. B6a, that we evaluated the calibration diameters at the intersections of the C-130 thresholds and the adjusted threshold–diameter table. At their greatest absolute relative departure, these calibrated diameters are 36% smaller than the values archived by NCAR for VOCALS and 12% larger than the values released for ICE-T. More typical relative departures are −5% (VOCALS) and +5% (ICE-T). Users of the VOCALS and ICE-T datasets are encouraged to use the threshold–diameter table provided in Table A1. This table is the basis of our analysis of the VOCALS C-130 PCASP measurements.

REFERENCES

Albrecht, B. A., 1989: Aerosols, cloud microphysics, and fractional cloudiness. *Science*, **245**, 1227–1230, doi:10.1126/science.245.4923.1227.

——, C. W. Fairall, D. W. Thomson, and A. B. White, 1990: Surface-based remote sensing of the observed and the adiabatic liquid water content of stratocumulus clouds. *Geophys. Res. Lett.*, **17**, 89–92, doi:10.1029/GL017i001p00089.

Austin, P., Y. Wang, V. Kujala, and R. Pincus, 1995: Precipitation in stratocumulus clouds: Observational and modeling results. *J. Atmos. Sci.*, **52**, 2329–2352, doi:10.1175/1520-0469(1995)052<2329:PISCOA>2.0.CO;2.

Baumgardner, D., J. E. Dye, G. B. Gandrud, and R. G. Knollenberg, 1992: Interpretation of measurements made by the forward scattering spectrometer probe (FSSP-300) during the Airborne Arctic Stratospheric Expedition. *J. Geophys. Res.*, **97**, 8035–8046, doi:10.1029/91JD02728.

Beheng, K. D., 1994: A parameterization of warm cloud microphysical conversion processes. *Atmos. Res.*, **33**, 193–206, doi:10.1016/0169-8095(94)90020-5.

Bohren, C. F., and B. A. Albrecht, 1998: *Atmospheric Thermodynamics*. Oxford University Press, 402 pp.

Brenguier, J.-L., and L. Chaumat, 2001: Droplet spectra broadening in cumulus clouds. Part I: Broadening in adiabatic cores. *J. Atmos. Sci.*, **58**, 628–641, doi:10.1175/1520-0469(2001)058<0628:DSBICC>2.0.CO;2.

——, and Coauthors, 2000: An overview of the ACE-2 cloudy column closure experiment. *Tellus*, **52B**, 815–827, doi:10.1034/j.1600-0889.2000.00047.x.

Bretherton, C. S., R. Wood, R. C. George, D. Leon, G. Allen, and X. Zheng, 2010: Southeast Pacific stratocumulus clouds, precipitation and boundary layer structure sampled along 20°S during VOCALS-REx. *Atmos. Chem. Phys.*, **10**, 10 639–10 654, doi:10.5194/acp-10-10639-2010.

Brown, E. N., C. A. Friehe, and D. H. Lenschow, 1983: The use of pressure fluctuations on the nose of an aircraft for measuring air motion. *J. Climate Appl. Meteor.*, **22**, 171–180, doi:10.1175/1520-0450(1983)022<0171:TUOPFO>2.0.CO;2.

Cai, Y., J. R. Snider, and P. Wechsler, 2013: Calibration of the passive cavity aerosol spectrometer probe for airborne determination of the size distribution. *Atmos. Meas. Tech.*, **6**, 2349–2358, doi:10.5194/amt-6-2349-2013.

Cerni, T. A., 1983: Determination of the size and concentration of cloud drops with an FSSP. *J. Climate Appl. Meteor.*, **22**, 1346–1355, doi:10.1175/1520-0450(1983)022<1346:DOTSAC>2.0.CO;2.

Charlson, R. J., F. P. J. Francisco, and J. H. Seinfeld, 2005: In search of balance. *Science*, **308**, 806–807, doi:10.1126/science.1108162.

Cooper, W. A., 1989: Effects of variable droplet growth histories on droplet size distributions. Part I: Theory. *J. Atmos. Sci.*, **46**, 1301–1311, doi:10.1175/1520-0469(1989)046<1301:EOVDGH>2.0.CO;2.

——, S. G. Lasher-Trapp, and A. M. Blyth, 2013: The influence of entrainment and mixing on the initial formation of rain in a warm cumulus cloud. *J. Atmos. Sci.*, **70**, 1727–1743, doi:10.1175/JAS-D-12-0128.1.

Davidovits, P., and Coauthors, 2004: Mass accommodation coefficient of water vapor on liquid water. *Geophys. Res. Lett.*, **31**, L22111, doi:10.1029/2004GL020835.

Frisch, A. S., C. W. Fairall, and J. B. Snider, 1995: Measurement of stratus cloud and drizzle properties in ASTEX with a K_α-band Doppler radar and microwave radiometer. *J. Atmos. Sci.*, **52**, 2788–2799, doi:10.1175/1520-0469(1995)052<2788:MOSCAD>2.0.CO;2.

Gerber, H., 1996: Microphysics of marine stratocumulus clouds with two drizzle modes. *J. Atmos. Sci.*, **53**, 1649–1662, doi:10.1175/1520-0469(1996)053<1649:MOMSCW>2.0.CO;2.

——, B. G. Arends, and A. S. Ackerman, 1994: A new microphysics sensor for aircraft use. *Atmos. Res.*, **31**, 235–252, doi:10.1016/0169-8095(94)90001-9.

Ghan, S. J., L. R. Leung, R. C. Easter, and H. Abdul-Razzak, 1997: Prediction of cloud droplet number in a general circulation model. *J. Geophys. Res.*, **102**, 21 777–21 794, doi:10.1029/97JD01810.

Guibert, S., J. R. Snider, and J.-L. Brenguier, 2003: Aerosol activation in marine stratocumulus clouds: 1. Measurement validation for a closure study. *J. Geophys. Res.*, **108**, 8628, doi:10.1029/2002JD002678.

Havlicek, L. L., and R. D. Crain, 1988: *Practical Statistics for the Physical Sciences*. American Chemical Society, 512 pp.

Hawkins, L. N., L. M. Russell, D. S. Covert, P. K. Quinn, and T. S. Bates, 2010: Carboxylic acids, sulfates, and organosulfates in processed continental organic aerosol over the southeast Pacific Ocean during VOCALS-Rex. *J. Geophys. Res.*, **115**, D13201, doi:10.1029/2009JD013276.

Hu, Y., and Coauthors, 2007: The depolarization-attenuated backscattering relation: CALIPSO lidar measurements vs. theory. *Opt. Express*, **15**, 5327–5332, doi:10.1364/OE.15.005327.

Hudson, J. G., 1984: Cloud condensation nuclei measurements within clouds. *J. Climate Appl. Meteor.*, **23**, 42–51, doi:10.1175/1520-0450(1984)023<0042:CCNMWC>2.0.CO;2.

——, and G. Svensson, 1995: Cloud microphysical relationships in California marine stratus. *J. Appl. Meteor.*, **34**, 2655–2666, doi:10.1175/1520-0450(1995)034<2655:CMRICM>2.0.CO;2.

——, and S. Yum, 1997: Droplet spectral broadening in marine stratus. *J. Atmos. Sci.*, **54**, 2642–2654, doi:10.1175/1520-0469(1997)054<2642:DSBIMS>2.0.CO;2.

——, and S. Nobel, 2014: CCN and vertical velocity influences on droplet concentrations and supersaturations in clean and polluted stratus clouds. *J. Atmos. Sci.*, **71**, 312–331, doi:10.1175/JAS-D-13-086.1.

——, ——, and V. Jha, 2012: Cloud droplet spectral width relationship to CCN spectra and vertical velocity. *J. Geophys. Res.*, **117**, D11211, doi:10.1029/2012JD017546.

——, S. Noble, and S. Tabor, 2015: Cloud supersaturations from CCN spectra Hoppel minima. *J. Geophys. Res. Atmos.*, **120**, 3436–3452, doi:10.1002/2014JD022669.

Iribarne, J. V., and W. L. Godson, 1981: *Atmospheric Thermodynamics.* 2nd ed. Reidel, 223 pp.

Jones, C. R., C. S. Bretherton, and D. Leon, 2011: Coupled vs. decoupled boundary layers in VOCALS-REx. *Atmos. Chem. Phys.*, **11**, 7143–7153, doi:10.5194/acp-11-7143-2011.

Klein, S. A., and D. L. Hartmann, 1993: The seasonal cycle of low stratiform clouds. *J. Climate*, **6**, 1587–1606, doi:10.1175/1520-0442(1993)006<1587:TSCOLS>2.0.CO;2.

Klett, J. D., 1981: Stable analytical inversion solution for processing lidar returns. *Appl. Opt.*, **20**, 211–220, doi:10.1364/AO.20.000211.

Korolev, A. V., 1995: The influence of supersaturation fluctuations on droplet size spectra formation. *J. Atmos. Sci.*, **52**, 3620–3634, doi:10.1175/1520-0469(1995)052<3620:TIOSFO>2.0.CO;2.

Kreidenweis, S. M., M. D. Petters, and P. J. DeMott, 2008: Single-parameter estimates of aerosol water content. *Environ. Res. Lett.*, **3**, 035002, doi:10.1088/1748-9326/3/3/035002.

Kuang, Z., and Y. L. Yung, 2000: Reflectivity variations off the Peru coast: Evidence for indirect effect of anthropogenic sulfate aerosols on clouds. *Geophys. Res. Lett.*, **27**, 2501–2504, doi:10.1029/2000GL011376.

Laaksonen, A., T. Vesala, M. Kulmala, P. M. Winkler, and P. E. Wagner, 2005: Commentary on cloud modelling and the mass accommodation coefficient of water. *Atmos. Chem. Phys.*, **5**, 461–464, doi:10.5194/acp-5-461-2005.

Leaitch, W. R., J. W. Strapp, and G. A. Isaac, 1986: Cloud droplet nucleation and cloud scavenging of aerosol sulfate in polluted atmospheres. *Tellus*, **38B**, 328–344, doi:10.1111/j.1600-0889.1986.tb00258.x.

Leon, D. C., Z. Wang, and D. Liu, 2008: Climatology of drizzle in marine boundary layer clouds based on 1 year of data from CloudSat and Cloud–Aerosol Lidar and Infrared Pathfinder Satellite Observations (CALIPSO). *J. Geophys. Res.*, **113**, D00A14, doi:10.1029/2008JD009835.

Liu, Y., and P. H. Daum, 2002: Anthropogenic aerosols: Indirect warming effect from dispersion forcing. *Nature*, **419**, 580–581, doi:10.1038/419580a.

——, and ——, 2004: Parameterization of the autoconversion process. Part I: Analytical formulations of the Kessler-type parameterizations. *J. Atmos. Sci.*, **61**, 1539–1548, doi:10.1175/1520-0469(2004)061<1539:POTAPI>2.0.CO;2.

Lu, M.-L., and J. H. Seinfeld, 2006: Effect of aerosol number concentration on cloud droplet dispersion: A large-eddy simulation study and implications for aerosol indirect forcing. *J. Geophys. Res.*, **111**, D02207, doi:10.1029/2005JD006419.

——, W. C. Conant, H. H. Jonsson, V. Varutbangkul, R. C. Flagan, and J. H. Seinfeld, 2007: The Marine Stratus/Stratocumulus Experiment (MASE): Aerosol–cloud relationships in marine stratocumulus. *J. Geophys. Res.*, **112**, D10209, doi:10.1029/2006JD007985.

McComiskey, A., G. Feingold, A. S. Frisch, D. D. Turner, M. A. Miller, J. C. Chiu, Q. Min, and J. A. Ogren, 2009: An assessment of aerosol–cloud interactions in marine stratus clouds based on surface remote sensing. *J. Geophys. Res.*, **114**, D09203, doi:10.1029/2008JD011006.

Meskhidze, N., A. Nenes, W. C. Conant, and J. H. Seinfeld, 2005: Evaluation of a new cloud droplet activation parameterization with in situ data from CRYSTAL-FACE and CSTRIPE. *J. Geophys. Res.*, **110**, D16202, doi:10.1029/2004JD005703.

Miles, N. L., J. Verlinde, and E. E. Clothiaux, 2000: Cloud droplet size distributions in low-level stratiform clouds. *J. Atmos. Sci.*, **57**, 295–311, doi:10.1175/1520-0469(2000)057<0295:CDSDIL>2.0.CO;2.

O'Connor, E. J., A. J. Illingworth, and R. J. Hogan, 2004: A technique for autocalibration of cloud lidar. *J. Atmos. Oceanic Technol.*, **21**, 777–786, doi:10.1175/1520-0426(2004)021<0777:ATFAOC>2.0.CO;2.

O'Dowd, C., D. Ceburnis, J. Ovadnevaite, A. Vaishya, M. Rinaldi, and M. C. Facchini, 2014: Do anthropogenic, continental or coastal aerosol sources impact on a marine aerosol signature at Mace Head? *Atmos. Chem. Phys.*, **14**, 10 687–10 704, doi:10.5194/acp-14-10687-2014.

Paltridge, G. W., 1980: Cloud–radiation feedback to climate. *Quart. J. Roy. Meteor. Soc.*, **106**, 895–899, doi:10.1002/qj.49710645018.

Particle Measuring Systems, 2002: PMS Model PCASP-100X 0.10–3.0 μm operating manual. PMS Inc., 45 pp.

Pawlowska, H., W. W. Grabowski, and J.-L. Brenguier, 2006: Observations of the width of cloud droplet spectra in stratocumulus. *Geophys. Res. Lett.*, **33**, L19810, doi:10.1029/2006GL026841.

Petters, M. D., and S. M. Kreidenweis, 2007: A single parameter representation of hygroscopic growth and cloud condensation nucleus activity. *Atmos. Chem. Phys.*, **7**, 1961–1971, doi:10.5194/acp-7-1961-2007.

Platt, C. M., and Coauthors, 1994: The Experimental Cloud Lidar Pilot Study (ECLIPS) for cloud–radiation research. *Bull. Amer. Meteor. Soc.*, **75**, 1635–1654, doi:10.1175/1520-0477(1994)075<1635:TECLPS>2.0.CO;2.

Politovich, M. K., 1993: A study of the broadening of droplet size distributions in cumuli. *J. Atmos. Sci.*, **50**, 2230–2244, doi:10.1175/1520-0469(1993)050<2230:ASOTBO>2.0.CO;2.

Rogers, R. R., and M. K. Yau, 1989: *A Short Course in Cloud Physics.* 3rd ed. Permagon Press, 304 pp.

Romakkaniemi, S., G. McFiggans, K. N. Bower, P. Brown, H. Coe, and T. W. Choularton, 2009: A comparison between trajectory ensemble and adiabatic parcel modeled cloud properties and evaluation against airborne measurements. *J. Geophys. Res.*, **114**, D06214, doi:10.1029/2008JD011286.

Shank, L. M., and Coauthors, 2012: Organic matter and nonrefractory aerosol over the remote Southeast Pacific: Oceanic and combustion sources. *Atmos. Chem. Phys.*, **12**, 557–576, doi:10.5194/acp-12-557-2012.

Snider, J. R., and J.-L. Brenguier, 2000: Cloud condensation nuclei and cloud droplet measurements during ACE-2. *Tellus*, **52B**, 828–842, doi:10.1034/j.1600-0889.2000.00044.x.

——, and M. D. Petters, 2008: Optical particle counter measurement of marine aerosol hygroscopic growth. *Atmos. Chem. Phys.*, **8**, 1949–1962, doi:10.5194/acp-8-1949-2008.

——, S. Guibert, J.-L. Brenguier, and J.-P. Putaud, 2003: Aerosol activation in marine stratocumulus clouds: 2. Köhler and parcel theory closure studies. *J. Geophy. Res.*, **108**, 8629, doi:10.1029/2002JD002692.

——, M. D. Petters, P. Wechsler, and P. Liu, 2006: Supersaturation in the Wyoming CCN instrument. *J. Atmos. Oceanic Technol.*, **23**, 1323–1339, doi:10.1175/JTECH1916.1.

——, and Coauthors, 2010: Intercomparison of CCN and hygroscopic fraction measurements: Coated soot particles investigated during the LACIS Experiment in November

(LExNo). *J. Geophys. Res.*, **115**, D11205, doi:10.1029/2009JD012618.

Stevens, B., G. Feingold, W. R. Cotton, and R. L. Walko, 1996: Elements of the microphysical structure of numerically simulated nonprecipitating stratocumulus. *J. Atmos. Sci.*, **53**, 980–1006, doi:10.1175/1520-0469(1996)053<0980:EOTMSO>2.0.CO;2.

Strapp, J. W., W. R. Leaitch, and P. S. K. Liu, 1992: Hydrated and dried aerosol-size-distribution measurements from Particle Measuring Systems FSSP-300 probe and the deiced PCASP-100X probe. *J. Atmos. Oceanic Technol.*, **9**, 548–555, doi:10.1175/1520-0426(1992)009<0548:HADASD>2.0.CO;2.

Tang, I. N., and H. R. Munkelwitz, 1994: Water activities, densities, and refractive indices of aqueous sulfates and sodium nitrate droplets of atmospheric importance. *J. Geophys. Res.*, **99**, 18 801–18 808, doi:10.1029/94JD01345.

TSI, 2000: Model 3080 Electrostatic Classifier instruction manual. TSI, Inc., Part 1933792, 147 pp.

——, 2012: Aerosol statistics lognormal distributions and $dN/dlogD_p$. TSI, Inc., Application Note PR-001, 6 pp. [Available online at http://www.tsi.com/uploadedFiles/_Site_Root/Products/Literature/Application_Notes/PR-001-RevA_Aerosol-Statistics-AppNote.pdf.]

Twohy, C. H., and Coauthors, 2013: Impacts of aerosol particles on the microphysical and radiative properties of stratocumulus clouds over the southeast Pacific Ocean. *Atmos. Chem. Phys.*, **13**, 2541–2562, doi:10.5194/acp-13-2541-2013.

Twomey, S., 1959: The nuclei of natural cloud formation. Part II: The supersaturation in natural clouds and the variation of cloud droplet concentration. *Geofis. Pura Appl.*, **43**, 243–249, doi:10.1007/BF01993560.

——, 1977: The influence of pollution on the shortwave albedo of clouds. *J. Atmos. Sci.*, **34**, 1149–1152, doi:10.1175/1520-0469(1977)034<1149:TIOPOT>2.0.CO;2.

Wang, J., P. H. Daum, S. S. Yum, Y. Liu, G. I. Senum, M.-L. Lu, J. H. Seinfeld, and H. Jonsson, 2009: Observations of marine stratocumulus microphysics and implications for processes controlling droplet spectra: Results from the Marine Stratus/Stratocumulus Experiment. *J. Geophys. Res.*, **114**, D18210, doi:10.1029/2008JD011035.

Wang, Z., and K. Sassen, 2001: Cloud type and macrophysical property retrieval using multiple remote sensors. *J. Appl. Meteor.*, **40**, 1665–1682, doi:10.1175/1520-0450(2001)040<1665:CTAMPR>2.0.CO;2.

——, P. Wechsler, W. Kuestner, J. French, A. Rodi, B. Glover, M. Burkhart, and D. Lukens, 2009: Wyoming Cloud Lidar: Instrument description and applications. *Opt. Express*, **17**, 13 576–13 587, doi:10.1364/OE.17.013576.

——, and Coauthors, 2012: Single aircraft integration of remote sensing and in situ sampling for the study of cloud microphysics and dynamics. *Bull. Amer. Meteor. Soc.*, **93**, 653–668, doi:10.1175/BAMS-D-11-00044.1.

Warner, J., 1969: The microstructure of cumulus cloud. Part II. The effect on droplet size distribution of the cloud nucleus spectrum and updraft velocity. *J. Atmos. Sci.*, **26**, 1272–1282, doi:10.1175/1520-0469(1969)026<1272:TMOCCP>2.0.CO;2.

Wood, R., K. K. Comstock, C. S. Bretherton, C. Cornish, J. Tomlinson, D. R. Collins, and C. Fairall, 2008: Open cellular structure in marine stratocumulus sheets. *J. Geophys. Res.*, **113**, D12207, doi:10.1029/2007JD009371.

——, and Coauthors, 2011a: The VAMOS Ocean–Cloud–Atmosphere–Land Study Regional Experiment (VOCALS-REx): Goals, platforms, and field operations. *Atmos. Chem. Phys.*, **11**, 627–654, doi:10.5194/acp-11-627-2011.

——, C. S. Bretherton, D. Leon, A. D. Clarke, P. Zuidema, G. Allen, and H. Coe, 2011b: An aircraft case study of the spatial transition from closed to open mesoscale cellular convection over the Southeast Pacific. *Atmos. Chem. Phys.*, **11**, 2341–2370, doi:10.5194/acp-11-2341-2011.

——, D. Leon, M. Lebsock, J. R. Snider, and A. D. Clarke, 2012: Precipitation driving of droplet concentration variability in marine low clouds. *J. Geophys. Res.*, **117**, doi:10.1029/2012JD018305.

Young, H. D., 1962: *Statistical Treatment of Experimental Data*. McGraw-Hill Book Company, 172 pp.

Yum, S. S., and J. G. Hudson, 2002: Maritime/continental microphysical contrasts in stratus. *Tellus*, **54B**, 61–73, doi:10.1034/j.1600-0889.2002.00268.x.

——, ——, and Y. Xie, 1998: Comparisons of cloud microphysics with cloud condensation nuclei spectra over the summertime Southern Ocean. *J. Geophys. Res.*, **103**, 16 625–16 636, doi:10.1029/98JD01513.

Zou, Y.-S., and N. Fukuta, 1999: The effect of diffusion kinetics on the supersaturation in clouds. *Atmos. Res.*, **52**, 115–141, doi:10.1016/S0169-8095(99)00025-3.

Zuidema, P., D. Leon, A. Pazmany, and M. Cadeddu, 2012: Aircraft millimeter-wave passive sensing of cloud liquid water vapor during VOCALS-Rex. *Atmos. Chem. Phys.*, **12**, 355–369, doi:10.5194/acp-12-355-2012.